COMMUNICATIONS IN NUMERICAL METHODS IN ENGINEERING
Commun. Numer. Meth. Engng 2006; **22**:1031–1065
Published online 28 April 2006 in Wiley InterScience (www.interscience.wiley.com). DOI: 10.1002/cnm.871

Coupling of mesh-free methods with finite elements: basic concepts and test results

T. Rabczuk[1,‡,‖], S. P. Xiao[2,*,†,¶] and M. Sauer[3,§]

[1]*Institute for Numerical Mechanics, University of Munich, Garching, Germany*
[2]*Department of Mechanical and Industrial Engineering, University of Iowa, Iowa City, U.S.A.*
[3]*Fraunhofer Institute for Short Time Dynamics, Ernst-Mach-Institute, Eckerstrasse 4, 79106 Freiburg, Germany*

SUMMARY

This paper reviews several novel and older methods for coupling mesh-free particle methods, particularly the element-free Galerkin (EFG) method and the smooth particle hydrodynamics (SPH), with finite elements (FEs). We study master–slave couplings where particles are fixed across the FE boundary, coupling via interface shape functions such that consistency conditions are satisfied, bridging domain coupling, compatibility coupling with Lagrange multipliers and hybrid coupling methods where forces from the particles are applied via their shape functions on the FE nodes and *vice versa*. The hybrid coupling methods are well suited for large deformations and adaptivity and the coupling procedure is independent of the particle distance and nodal arrangement. We will study the methods for several static and dynamic applications, compare the results to analytical and experimental data and show advantages and drawbacks of the methods. Copyright © 2006 John Wiley & Sons, Ltd.

KEY WORDS: mesh-free particle methods; adaptivity; EFG; SPH

1. INTRODUCTION

Mesh-free methods became a good alternative to FEM and FDM in certain areas. For problems involving large deformation, fracture and fragmentation, mesh-free methods seem to be more flexible than finite elements (FEs), because they do not rely on a fixed topological connectivity between nodes. Mesh-free methods have advantages in problems involving crack growth as

*Correspondence to: S. P. Xiao, Department of Mechanical and Industrial Engineering, University of Iowa, Iowa City, U.S.A.
†E-mail: shaoping-xiao@uiowa.edu
‡E-mail: Timon.Rabczuk@lnm.mur.tum.de
§E-mail: sauer@emi.fhg.de
¶Assistant Professor.
‖Research Fellow.

Contract/grant sponsor: Publishing Arts Research Council; contract/grant number: 98-1846389

Received 25 October 2005
Revised 2 March 2006
Accepted 3 March 2006

no remeshing is necessary. Particles can be added without the need to remesh, so adaptive refinement of the discretization can be done easily.

Considerable research in mesh-free methods has been devoted on inherent difficulties like consistency, stability and Dirichlet boundary conditions. While these issues are not yet completely resolved, viable methods are available. In addition, up to now, the computational effort for mesh-free methods is higher than for FEs. Hence, as long as no robust and, at the same time, efficient formulation for mesh-free particle methods is available, it seems beneficial to discretize only certain parts of the domain with particles and the rest with FEs. Within this article, we will review some selected coupling approaches in detail. A good overview about inter alia coupling methods can be found in the book of Li and Liu [1].

One of the first coupling procedures for mesh-free particle methods and FEs was proposed by Attaway *et al.* [2]. They developed a master–slave coupling for fluid–structure interactions; the fluid was discretized with particles, the structure was modelled with FEs. Their algorithm is based on a common master–slave coupling (see Reference [3]); in every time step they checked whether particles penetrate element faces. The calculated forces that prevent the interpenetration are always normal to the corresponding element surface. Sliding between particles and elements in tangential direction is allowed. A similar approach was proposed by Johnson [4] and Johnson *et al.* [5]. In addition, they developed transition elements where particles are fixed to FE nodes. This allows for a rigid coupling in the sense that tensile and shear forces are transferred through the interface. We will propose here a new approach where the particles are rigidly fixed to the FE nodes via a master–slave coupling as described in Reference [3].

Liu *et al.* [6, 7] showed how to couple the reproducing kernel particle method (RKPM) with finite element method (FEM) by modifying the shape functions in the transition area for both RKPM and FEM. They applied the reproducing condition also in the transition area. Belytschko *et al.* [8] developed a coupling algorithm for element-free Galerkin (EFG) and FEM by a mixed interpolation in the transition domain, where FE nodes are substituted by particles and connected via ramp functions to the EFG nodes so that continuity and consistency are preserved on the interface elements. In Reference [9] they extended this method also for a nodal integration of EFG. The drawback of this method is that the derivatives are discontinuous along the *interface*.

Huerta *et al.* [10, 11] developed a mixed hierarchical approximation based on finite element and mesh-free methods. They enriched both FE and EFG method and were able to remove the discontinuities in the derivative across the *interior* boundaries that was the major drawback of the method in Reference [8].

Hegen [12] coupled FEM and EFG with Lagrange multipliers for elasto-static problems. In his approach, the substitution of FE nodes by particles is not necessary. Rabczuk and Belytschko [13] extended this idea to non-linear problems and applied it to deformable interfaces. Karutz [14] showed convergence of a similar approach to model crack-propagation problems using an adaptively generated EFG domain. A coupling with Lagrange multipliers where FEs and particles overlap was invented by Belytschko and Xiao [15]. They called this method the 'bridging domain coupling method' and successfully applied it to atomic and multiscale simulations. Another bridging domain coupling was before proposed by Wagner and Liu [16] to couple atomic and continuum simulations, see also Reference [17] for a more comprehensive overview. While the bridging domain coupling in Reference [15] suffered from spurious wave reflections in certain cases, Kadowaki and Liu [18, 19] introduced some wave reflection algorithms to remove this drawback.

Sauer [20] proposed an smooth particle hydrodynamics–finite element (SPH–FE) coupling by extending the SPH domain onto the FE mesh. Different possibilities for exchanging forces between FE nodes and particles were shown, and the approach was used for adaptive conversion of elements into particles. The main difference with most above-mentioned methods is that they used a *strong-form* coupling.

Recently, the group around Liu and Li [21–23] developed a hybrid method called reproducing kernel element method (RKEM), which exploits advantages of both, mesh-free and FE methods, e.g. the RKEM shape functions fulfil the Kronecker delta property. A similar method (moving particle FEM) was developed almost simultaneously by Hao *et al.* [24]. While most hybrid FE–mesh-free methods are at least first-order in convergence, Liu *et al.* [21] showed that their RKEM method maintains the usual convergence rate. Another method to maintain the usual convergence rate by hierarchical enrichment was proposed by Wagner and Liu [25] and Han *et al.* [26]. Other good overviews about mesh-free and particle methods, their coupling to FEs with impressive examples can be found in Li and Liu [1, 27–37].

This article is arranged as follows. We will briefly review the EFG- and SPH-method and FE shape function. Then we will describe the coupling approaches tested in our article, i.e. master–slave couplings, coupling via mixed interpolation, coupling via Lagrange multipliers, bridging domain coupling and hybrid couplings. We will compare these methods for two examples where an analytical solution is available: in statics, the cantilever beam and in dynamics, a rod with initial boundary conditions. The last example was studied by Rabczuk *et al.* [38] for different mesh-free methods. We will further apply the methods to several static and dynamic problems where experimental data are available and discuss some advantages and drawbacks of the different methods.

2. BASIC EQUATIONS

The basic equations of continuum mechanics in a total Lagrangian description are the conservation of mass

$$\varrho J = \varrho_0 \, J_0 \tag{1}$$

the conservation of linear momentum

$$\ddot{\mathbf{u}} = \frac{1}{\varrho_0} \nabla \cdot \mathbf{P} + \mathbf{b} \tag{2}$$

and the conservation of angular momentum

$$\mathbf{F} \cdot \mathbf{P} = \mathbf{P}^{\mathrm{T}} \cdot \mathbf{F}^{\mathrm{T}} \tag{3}$$

where J and J_0 is the Jacobian and initial Jacobian, $\mathbf{u}$ is the displacement vector, ϱ_0 is the initial density, $\mathbf{P}$ are the nominal stresses, $\mathbf{b}$ are the body forces and $\mathbf{F}$ denotes the deformation gradient. The superimposed dot indicates the material time derivatives and the superscript 'T' denotes the transpose of a tensor or a vector.

The boundary conditions are

$$\mathbf{u}(\mathbf{X}, t) = \bar{\mathbf{u}}(\mathbf{X}, t) \quad \text{on } \Gamma_0^u \tag{4}$$

$$\mathbf{n}^0 \cdot \mathbf{P}(\mathbf{X}, t) = \bar{\mathbf{t}}(\mathbf{X}, t) \quad \text{on } \Gamma_0^t \tag{5}$$

where $\bar{\mathbf{u}}$ and $\bar{\mathbf{t}}$ are the prescribed displacement and traction, respectively, $\mathbf{n}^0$ is the outward normal to the domain in the initial configuration and $\Gamma_0^u \cup \Gamma_0^t = \Gamma_0$, $\Gamma_0^u \cap \Gamma_0^t = 0$.

3. SHAPE FUNCTIONS

In any of the approximation methods we consider the approximation of the trial functions by

$$\mathbf{u}(\mathbf{X}, t) = \sum_{I=1}^{N} N_I(\mathbf{X})\mathbf{u}_I(t) \tag{6}$$

where $N_I(\mathbf{X})$ is a shape function and $\mathbf{u}_I$ is a parameter associated with node $\mathbf{X}_I$. For interpolants, such as FE shape functions $\mathbf{u}(\mathbf{X}_I, t) = \mathbf{u}_I(t)$. The test functions are approximated by

$$\delta\mathbf{u}(\mathbf{X}) = \sum_{I=1}^{N} N_I(\mathbf{X})\delta\mathbf{u}_I \tag{7}$$

We have chosen the same shape functions for the approximation of the test and trial functions.

3.1. FE shape functions

Within this paper, we restrict ourselves to two-dimensional problems. The standard bilinear shape functions for two-dimensional four-node FEs are

$$N_I(\boldsymbol{\xi}) = 1/4(1 + \xi_I\xi)(1 + \eta_I\eta) \tag{8}$$

where $\mathbf{X}(\boldsymbol{\xi})$ is a mapping from the parent domain of problem to the physical domain and ξ_I and η_I are the nodal co-ordinates in the parent domain $\xi \in [-1, 1], \eta \in [-1, 1]$, given by

$$\mathbf{X} = \sum_{I=1}^{N} \mathbf{X}_I N_I \tag{9}$$

3.2. Mesh-free shape functions

In the literature there exists a large amount of mesh-free particle methods. As already mentioned, we consider the EFG- and SPH-method [39–43] although the coupling ideas presented in this paper are, in general, applicable to most mesh-free methods. A Lagrangian kernel is chosen, i.e. the shape functions are evaluated in the reference configuration only.

3.2.1. SPH shape functions. In standard SPH, the shape function is a product of particle volume and a weighting function:

$$N(\mathbf{X}) = \Delta V_I W(\mathbf{X} - \mathbf{X}_I, h_0) \tag{10}$$

where ΔV_I is the volume associated with the neighbour particle and $W(\mathbf{X} - \mathbf{X}_I, h_0)$ is a weighting function.

3.2.2. EFG shape functions. The EFG shape functions are given by

$$N(\mathbf{X}) = \mathbf{p}(\mathbf{X}) \cdot A(\mathbf{X})^{-1} \cdot \mathbf{p}_j W(\mathbf{X} - \mathbf{X}_I, h_0) \tag{11}$$

with

$$A(\mathbf{X}) = \sum_{I=1}^{N} p_j p_j^{\mathrm{T}} W(\mathbf{X} - \mathbf{X}_I, h_0) \tag{12}$$

where $\mathbf{p}(\mathbf{X})$ are basis functions which are chosen to $\mathbf{p}(\mathbf{X}) = (1\ X\ Y\ Z)$ to fulfil linear completeness (see Reference [9]). When the base functions are chosen to $p(\mathbf{X}) = (1)$, they are known as Shepard functions and denoted by w in the following.

4. QUADRATURE FOR FINITE ELEMENT AND PARTICLE METHODS

For the FEM method, the integrals are customarily evaluated by Gauss quadrature:

$$\int_{\Omega_0} u(\mathbf{X})\, \mathrm{d}\Omega_0 = \int_{-1}^{+1} \int_{-1}^{+1} u(\xi)\, \frac{1}{8} \det \mathbf{J}(\xi)\, \mathrm{d}\xi = \sum_{J=1}^{N_{\mathrm{GP}}} w_P u_p(\xi)\, \frac{1}{8} \det \mathbf{J}_p(\xi) \tag{13}$$

where ξ indicates the co-ordinates of the local element co-ordinate system, $\mathbf{J}$ is the Jacobian determinant and w_p are the weighting coefficients which depend on the number of Gauss points in the cell. The Jacobian matrix $\mathbf{J} = \partial \mathbf{x} / \partial \xi$ follows from (9)

$$\mathbf{J} = \sum_{J=1}^{N_{\mathrm{GP}}} \frac{\partial N_J(\xi)}{\partial \xi}\, \mathbf{x}_J \tag{14}$$

The bilinear shape functions mentioned in Equation (8) can be integrated exactly using a 2×2 quadrature. In this work, however, we use the common reduced integration scheme with only one integration point in the element centre which is computationally cheaper.

For the particle methods we use an integration by stress points, see, e.g. Reference [44]. Stress point integration removes the instability due to rank deficiency, which is obtained in a pure nodal integration but retains the mesh-free character of the method.

5. COUPLING PROCEDURES OF MESH-FREE PARTICLE METHODS AND FEM

5.1. Master–slave coupling approaches

5.1.1. Coupling by fixing particles to the FE nodes. Johnson *et al.* [4] fixed the particles to the FE nodes by a simple procedure. In their method, the forces on the FE nodes $\mathbf{F}_K$ and the particles $\mathbf{F}_P$ as well as their masses and the calculation of the common accelerations are combined. The forces which act on the nodes and particles are given by

$$\mathbf{F}_K = m_K \mathbf{a}_K, \quad \mathbf{F}_P = m_P \mathbf{a}_P \tag{15}$$

and are determined by the (already) calculated accelerations. The common acceleration of the node and corresponding particle is

$$\mathbf{a}_{K,\text{coupling}} = \mathbf{a}_{P,\text{coupling}} = \frac{\mathbf{F}_K + \mathbf{F}_P}{m_K + m_P} \tag{16}$$

One major drawback is that every particle needs a corresponding node and *vice versa*, so that the coupling is not valid for an arbitrary particle arrangement.

5.1.2. Master–slave coupling. We consider here another possibility to fix the particles rigidly to the elements so that an arbitrary nodal arrangement is possible. We follow a master–slave procedure as explained in Reference [3]. In this coupling method, the particles adjacent to the FEM model are rigidly connected to the FEM interface (see Figure 1). Therefore, the particles are considered as slave nodes while the FEM nodes are the master nodes. As proposed in Reference [3] the slave nodes are updated after master nodes have been updated in an explicit method.

In the initialization, the co-ordinates of the closest point projection of the initial position of each particle P on the FE/mesh-free interface has to be obtained as illustrated in Figure 2. For convenience, a generic surface with element co-ordinates (ξ_c, η_C) on the surface is considered, assumed that $\xi = \pm 1$. In the first step, the element co-ordinates of the projection of particle P onto the element surface, denoted by C, must be found (see Figure 2), it corresponds to the closest point projection of P onto C. The location of this point at any time can be found by

$$\mathbf{x} = \sum_{J=1}^{N} N_I(\xi_C, \eta_C, \pm 1)\mathbf{x}_I \tag{17}$$

The velocities of the point C are given at any time by

$$\mathbf{v} = \sum_{J=1}^{N} N_I(\xi_C, \eta_C, \pm 1)\mathbf{v}_I \tag{18}$$

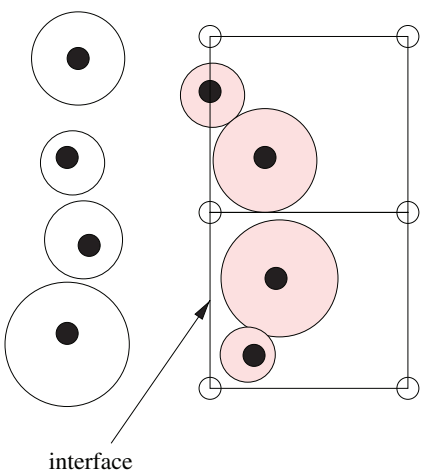

Figure 1. Two-dimensional illustration of particle/FEM interaction, grey particles are slave.

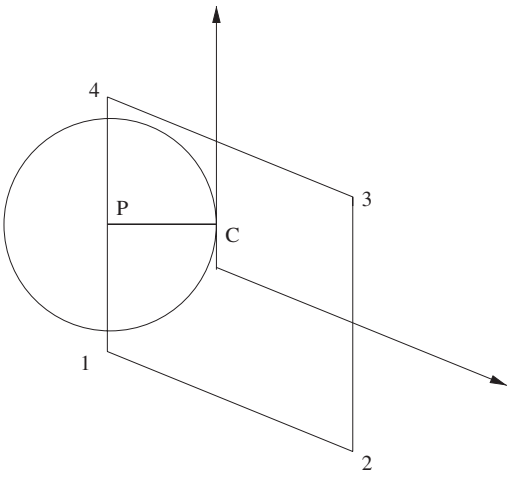

Figure 2. Projection of particle centre P onto interface to finite elements.

To obtain the velocities of the particles the master–slave algorithm (see Reference [3]) is applied. Since P is a slave node, its velocities at any time can be expressed in terms of the velocities of the nodes I of the FE ($I = 1, \ldots, 4$). The relationship will be done in two steps. First, $\mathbf{v}_P^{\mathrm{S}}$ is expressed in terms of $\mathbf{v}_C^{\mathrm{S}}$, then $\mathbf{v}_C^{\mathrm{S}}$ in terms of the master nodes $\mathbf{v}_I^{\mathrm{M}}$ where the superscripts S and M denote slave and master nodes, respectively. Since PC is a line in a rigid body, the velocity of the slave particle are given by

$$\mathbf{v}_P^{\mathrm{S}} = \mathbf{v}_C^{\mathrm{S}} + \boldsymbol{\omega}(\mathbf{x}_P - \mathbf{x}_C), \quad \boldsymbol{\omega}_P = \boldsymbol{\omega}_C \tag{19}$$

when $\boldsymbol{\omega}$ denotes the angular velocity of the line PC. The above can be written in matrix form as:

$$\begin{bmatrix} \mathbf{v}_P^{\mathrm{S}} \\ \boldsymbol{\omega}_P^{\mathrm{S}} \end{bmatrix} = \begin{bmatrix} \mathbf{I} & \boldsymbol{\Omega}_{PC} \\ 0 & \mathbf{I} \end{bmatrix} \begin{bmatrix} \mathbf{v}_C \\ \boldsymbol{\omega}_C \end{bmatrix} \tag{20}$$

We define

$$\mathbf{T}_1 = \begin{bmatrix} \mathbf{I} & \boldsymbol{\Omega}_{PC} \\ 0 & \mathbf{I} \end{bmatrix} \tag{21}$$

where

$$\boldsymbol{\Omega}_{PC} = \begin{bmatrix} 0 & z_{PC} & y_{PC} \\ -z_{PC} & 0 & x_{PC} \\ -y_{PC} & -x_{PC} & 0 \end{bmatrix} \tag{22}$$

The velocity of point C can be expressed in terms of the shape functions of the surface nodes:

$$\mathbf{v}_C = \sum_{J=1}^{N} N_I(\xi, \eta, 1)\mathbf{v}_I^{\mathrm{M}}, \quad \boldsymbol{\omega}_C = \sum_{J=1}^{N} \mathbf{A}_I \mathbf{v}_I^{\mathrm{M}} \tag{23}$$

where $\mathbf{A}$ will be defined later, see Equations (29) and (30).

Combining these, we have

$$\begin{bmatrix} \mathbf{v}_C \\ \boldsymbol{\omega}_C \end{bmatrix} = \begin{bmatrix} \mathbf{N}_I \mathbf{I} \\ \mathbf{A}_I \end{bmatrix} [\mathbf{v}_I^{\mathrm{M}}] \tag{24}$$

where

$$\mathbf{T}_2 = \begin{bmatrix} \mathbf{N}_I \mathbf{I} \\ \mathbf{A}_I \end{bmatrix} \tag{25}$$

Considering the particle velocities at point P and C we obtain

$$\begin{bmatrix} \mathbf{v}_P^{\mathrm{S}} \\ \boldsymbol{\omega}_P^{\mathrm{S}} \end{bmatrix} = \sum_{J=1}^{N} \mathbf{T}_1 \mathbf{T}_2 \mathbf{v}_I^{\mathrm{M}} \tag{26}$$

where

$$\mathbf{T}_I = \mathbf{T}_1 \begin{bmatrix} N_I(\xi_C, \eta_C, \pm 1) \\ \mathbf{A}_I(\xi_C, \eta_C, \pm 1) \end{bmatrix} \tag{27}$$

From work conjugacy, it follows that any nodal forces on particle P should be transformed and added to node I, so

$$\mathbf{f}_I^{\mathrm{M}} = \sum_{J \in S} \mathbf{T}_J^{\mathrm{T}} \begin{bmatrix} \mathbf{f}_P^{\mathrm{S}} \\ \mathbf{m}_P^{\mathrm{S}} \end{bmatrix} \quad \forall J \in S \tag{28}$$

where J are the supporting nodes in the domain S. The angular velocity can be calculated by dividing the quadrilateral surface into two triangles as shown in Figure 3. Then, the normal

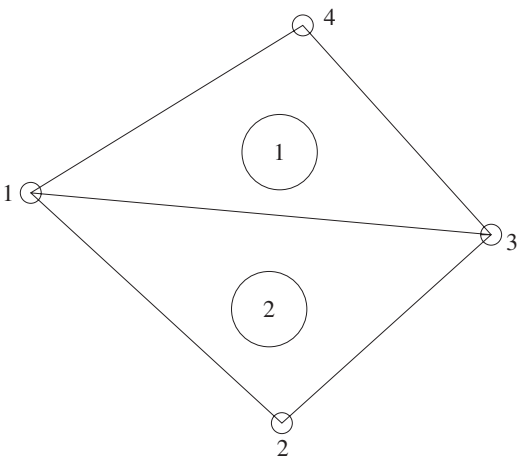

Figure 3. Computation of the angular velocity in terms of the normal.

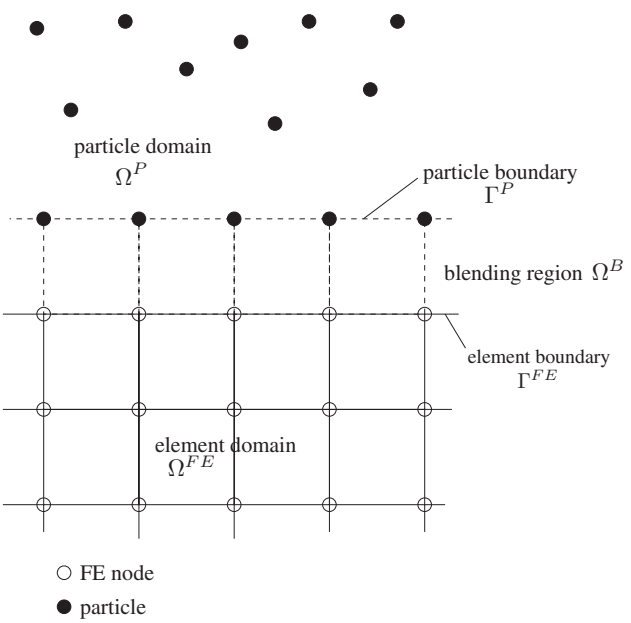

Figure 4. Coupling of finite elements and particles via ramp functions.

$\mathbf{n}$ of the triangle $\overline{123}$ is given by

$$\mathbf{n} = \frac{\mathbf{x}_{12} \times \mathbf{x}_{31}}{\|\mathbf{x}_{12} \times \mathbf{x}_{31}\|} \tag{29}$$

so that the angular velocity is

$$\boldsymbol{\omega} = \dot{\mathbf{n}} \tag{30}$$

with

$$\dot{\mathbf{n}} = (\mathbf{n}^{t+\triangle t} - \mathbf{n}^t)/\triangle t \tag{31}$$

5.2. *Compatibility coupling (coupling via ramp functions)*

Consider a domain of problem with a hybrid discretization between FEs and particles as illustrated in Figure 4. The superscripts FE and P indicate the domain for the FEs and particles, respectively. The transition region is designated by Ω^{B}, Ω^{P} denotes the particle domain and Ω^{FE} is the element domain. The element and particle boundary is Γ^{FE} and Γ^{P}, respectively. The weak form of the momentum equation is the standard principle of virtual work: find $\mathbf{u} \in \mathscr{V}$ such that

$$\delta W = \delta W_{\mathrm{int}} - \delta W_{\mathrm{ext}} + \delta W_{\mathrm{kin}} = 0 \quad \forall \delta \mathbf{u} \in \mathscr{V}_0 \tag{32}$$

where

$$\mathscr{V} = \{\mathbf{u}(\cdot,t) | \mathbf{u}(\cdot,t) \in \mathscr{H}^1,\ \mathbf{u}(\cdot,t) = \bar{\mathbf{u}}(t) \text{ on } \Gamma_0^u\} \tag{33}$$

$$\mathscr{V}_0 = \{\delta\mathbf{u} | \delta\mathbf{u} \in \mathscr{V},\ \delta\mathbf{u} = 0 \text{ on } \Gamma_u\}$$

$$\delta W_{\text{int}} = \int_{\Omega_0} (\nabla_0 \otimes \delta\mathbf{u})^{\text{T}} : \mathbf{P}\, \text{d}\Omega_0 \tag{34}$$

$$\delta W_{\text{ext}} = \int_{\Omega_0} \varrho_0 \mathbf{b} \cdot \delta\mathbf{u}\, \text{d}\Omega_0 + \int_{\Gamma_0^t} \bar{\mathbf{t}}_0 \cdot \delta\mathbf{u}\, \text{d}\Gamma_0 \tag{35}$$

$$\delta W_{\text{kin}} = \int_{\Omega_0} \varrho_0 \delta\mathbf{u} \cdot \ddot{\mathbf{u}}\, \text{d}\Omega_0 \tag{36}$$

where the prefix δ denotes the test function and W_{ext} is the external energy, W_{int} the internal energy and W_{kin} the kinetic energy. The approximation of the trial functions is given in Section 3. The test functions have a similar structure. In the interface region, an approximation is given by

$$\mathbf{u}^h = \mathbf{u}^{\text{FE}}(\mathbf{X}) + R(\mathbf{X})(\mathbf{u}^{\text{P}}(\mathbf{X}) - \mathbf{u}^{\text{FE}}(\mathbf{X})), \quad \mathbf{X} \in \Omega^{\text{B}} \tag{37}$$

where $\mathbf{u}^{\text{FE}}$ and $\mathbf{u}^{\text{P}}$ are the FE and particle approximations for $\mathbf{u}$ in the transition region and $R(\mathbf{X})$ is a ramp function, so that $R(\mathbf{X}) = 1, \mathbf{X} \in \Gamma_{\text{P}}$ and $R(\mathbf{X}) = 0, \mathbf{X} \in \Gamma_{\text{FE}}$. It is constructed with the use of a linear ramp function along the interface element boundaries so that continuity is ensured:

$$R(\mathbf{X}) = 3r^2(\mathbf{X}) - 2r^3(\mathbf{X}) \tag{38}$$

with

$$r(\mathbf{X}) = \sum_{J \in S_{\Gamma^{\text{P}}}} N_J(\mathbf{X}) \tag{39}$$

where $S_{\Gamma^{\text{P}}}$ is the set of nodes on Γ^{P}. Substituting the FE approximations and the mesh-free approximation into Equation (39) the approximation in the transition region is obtained:

$$\mathbf{u}^h(\mathbf{X}) = \sum_J \tilde{N}_I(\mathbf{X})\mathbf{u}_I, \quad \mathbf{X}_I \in \Omega^{\text{B}} \tag{40}$$

with the interface shape function

$$\tilde{N}_I(\mathbf{X}) = (1 - R(\mathbf{X}))N_I(\boldsymbol{\xi}(\mathbf{X})) + R(\mathbf{X})N_I(\mathbf{X}) \quad \mathbf{X} \in \Omega^{\text{B}} \tag{41}$$

$$\tilde{N}_I(\mathbf{X}) = R(\mathbf{X})N_I(\mathbf{X}) \quad \mathbf{X} \notin \Omega^{\text{B}} \tag{42}$$

In Reference [8] it is proven that linear completeness is preserved in the whole domain. If the integrals for the particles are evaluated by a nodal integration with stress points, the shape functions in the blending domain have only to be evaluated at the particle boundary Γ^{P} and

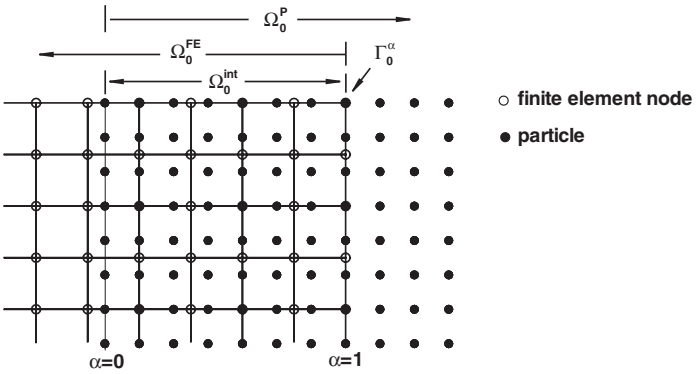

Figure 5. Finite element model coupled with particle method.

element boundary Γ^{FE} and are reduced to:

$$\tilde{N}_I(\mathbf{X}) = N_I(\mathbf{X}) \quad \mathbf{X} \in \Omega^{\mathrm{B}} \text{ on } \Gamma^{\mathrm{FE}} \tag{43}$$

$$\tilde{N}_I(\mathbf{X}) = 0 \quad \mathbf{X} \notin \Omega^{\mathrm{B}} \text{ on } \Gamma^{\mathrm{FE}} \tag{44}$$

$$\tilde{N}_I(\mathbf{X}) = N(\mathbf{X}) \quad \mathbf{X} \notin \Omega^{\mathrm{B}} \text{ on } \Gamma^{\mathrm{P}} \tag{45}$$

since $R(\mathbf{X}) = 1$ on Γ^{P} and $R(\mathbf{X}) = 0$ on Γ^{FE}. The approximation of the test functions in the blending region has the same structure. They are inserted in the weak form of the linear momentum equation.

5.3. *Bridging domain coupling method*

5.3.1. coupling model. We denote the complete domain in the initial configuration by Ω_0 and its boundaries by Γ_0; Γ_0 consists of traction boundaries Γ_0^t and the displacement boundaries Γ_0^u. The domains are subdivided into the subdomains treated by FEMs, Ω_0^{FE}, and that treated by particle methods, Ω_0^{P}; the latter is the domain encompassed by the particles of the model. The intersection of these two domains is denoted by Ω_0^{int} in the initial configuration, Ω^{int} in the current configuration; Ω^{int} is often called the overlapping subdomain (or bridging domain), see Reference [15]; Γ_0^{α} denotes the edge of the FE domain; an example of a model is shown in Figure 5.

In expressing the total internal potential energy of the system we employ a scaling parameter α in the overlapping subdomain. The parameter α is defined as $\alpha = l(\mathbf{X})/l_0$ where $l(\mathbf{X})$ is the least square of projection of $\mathbf{X}$ onto Γ_0^{α} as shown in Figure 5. The scaling parameter α is unity at the edge of the FE domain and vanishes at the other edge of Ω_0^{int}; it is important that Ω_0^{int} includes the last line of particles.

In the absence of heat transmission the conservation of energy of governing equations in the entire domain is

$$W^{\mathrm{int}} = \int_{\Omega_0^{\mathrm{FE}}} \beta^{\mathrm{FE}} \mathbf{F}^{\mathrm{T}} \cdot \mathbf{P} \, \mathrm{d}\Omega_0^{\mathrm{FE}} + \int_{\Omega_0^{\mathrm{P}}} \beta^{\mathrm{P}} \mathbf{F}^{\mathrm{T}} \cdot \mathbf{P} \, \mathrm{d}\Omega_0^{\mathrm{P}} \tag{46}$$

where the scaling multiplier field β is defined as

$$\beta^{\mathrm{FE}}(\mathbf{X}) = \begin{cases} 0 & \text{in } \Omega_0^{\mathrm{P}} \\ 1-\alpha & \text{in } \Omega_0^{\mathrm{int}} \\ 1 & \text{in } \Omega_0^{\mathrm{FE}} - \Omega_0^{\mathrm{int}} \end{cases} \tag{47}$$

$$\beta^{\mathrm{P}}(\mathbf{X}) = \begin{cases} 0 & \text{in } \Omega_0^{\mathrm{FE}} \\ \alpha & \text{in } \Omega_0^{\mathrm{int}} \\ 1 & \text{in } \Omega_0^{\mathrm{P}} - \Omega_0^{\mathrm{int}} \end{cases} \tag{48}$$

The external energy is

$$W^{\mathrm{ext}} = \int_{\Omega_0^{\mathrm{FE}}} \beta^{\mathrm{FE}} \rho_0 \mathbf{b} \cdot \mathbf{u}\, \mathrm{d}\Omega_0^{\mathrm{FE}} + \int_{\Omega_0^{\mathrm{P}}} \beta^{\mathrm{P}} \rho_0 \mathbf{b} \cdot \mathbf{u}\, \mathrm{d}\Omega_0^{\mathrm{P}} + \int_{\Gamma_0^{\mathrm{FE}}} \beta^{\mathrm{FE}} \bar{\mathbf{t}} \cdot \mathbf{u}\, \mathrm{d}\Gamma_0^{\mathrm{FE}} + \int_{\Gamma_0^{\mathrm{P}}} \beta^{\mathrm{P}} \bar{\mathbf{t}} \cdot \mathbf{u}\, \mathrm{d}\Gamma_0^{\mathrm{P}} \tag{49}$$

In Ω_0^{int} the displacements can be approximated in the terms of shape functions $N_I(\mathbf{X})$ of FEM or kernel functions $w_I(\mathbf{X})$ of particle methods, respectively, by

$$\mathbf{u}^{\mathrm{FE}}(\mathbf{X}, t) = \sum_I N_I(\mathbf{X}) \mathbf{u}_I^{\mathrm{FE}}(t) \tag{50}$$

$$\mathbf{u}^{\mathrm{P}}(\mathbf{X}, t) = \sum_I w_I(\mathbf{X}) \mathbf{u}_I^{\mathrm{P}}(t) \tag{51}$$

Therefore, the constraints condition in Ω_0^{int} at the discrete position of particles is

$$\mathbf{g}_I = \{g_{iI}\} = \{u_{iI}^{\mathrm{FE}} - u_{iI}^{\mathrm{P}}\} = \left\{ \sum_J N_{JI} u_{iJ}^{\mathrm{FE}} - \sum_K w_{KI} u_{iK}^{\mathrm{P}} \right\} \tag{52}$$

The Lagrange multiplier field is also expressed in terms of shape functions denoted by $\Lambda_I(\mathbf{X})$:

$$\lambda_i(\mathbf{X}, t) = \sum_I \Lambda_I(\mathbf{X}) \bar{\lambda}_{iI}(t) \tag{53}$$

Generally, the shape functions for the Lagrange multiplier field $\Lambda_I(\mathbf{X})$ will differ from that for the displacement, $N_I(\mathbf{X})$ or $w_I(\mathbf{X})$, and they must satisfy the LBB conditions. The Lagrange multiplier field is usually represented by inserting FEs in the intersection domain and the FE approximation is applied on the particles of the overlapping subdomain. To distinguish the Lagrange multiplier field λ_i in Equation (53), $\bar{\lambda}_{iI}$ is denoted as the unknown Lagrange multiplier at the Lagrange multiplier nodes.

5.3.2. Discrete equations. The energy function for augmented Lagrangian method is

$$W_{\mathrm{AL}} = W^{\mathrm{int}} - W^{\mathrm{ext}} + \boldsymbol{\lambda}^{\mathrm{T}} \mathbf{g} + \tfrac{1}{2} p \mathbf{g}^{\mathrm{T}} \mathbf{g} \tag{54}$$

where p is the penalty parameter. If $p = 0$, Equation (54) will be identical to the expression of energy function for Lagrange multiplier method.

The discrete equations are then obtained by setting the derivatives of W_{AL} with respect to $\mathbf{u}_I$ and λ_I to zero. This gives

$$\frac{\partial W_{\mathrm{AL}}}{\partial u_{iI}^{\mathrm{FE}}} = (F_{iI}^{\mathrm{int}} - F_{iI}^{\mathrm{ext}}) + \sum_L \left[\left(\sum_K \Lambda_{KL} \bar{\lambda}_K \right) N_{IL} \right] + p \sum_L \left[\left(\sum_K N_{KL} u_{iK}^{\mathrm{FE}} - \sum_K w_{KL} u_{iK}^{\mathrm{P}} \right) N_{IL} \right] = 0 \tag{55}$$

$$\frac{\partial W_{\mathrm{AL}}}{\partial u_{iI}^{\mathrm{P}}} = (f_{iI}^{\mathrm{int}} - f_{iI}^{\mathrm{ext}}) - \sum_L \left[\left(\sum_K \Lambda_{KL} \bar{\lambda}_K \right) w_{IL} \right] - p \sum_L \left[\left(\sum_K N_{KL} u_{iK}^{\mathrm{FE}} - \sum_K w_{KL} u_{iK}^{\mathrm{P}} \right) w_{IL} \right] = 0 \tag{56}$$

$$\frac{\partial W_{\mathrm{AL}}}{\partial \bar{\lambda}_{iI}} = \sum_L \Lambda_{IL} \left[\sum_K N_{KL} u_{iK}^{\mathrm{FE}} - \sum_K w_{KL} u_{iK}^{\mathrm{P}} \right] = 0 \tag{57}$$

where

$$N_{KI} = N_K(\mathbf{X}_I), \quad \Lambda_{KI} = \Lambda_K(\mathbf{X}_I) \tag{58}$$

$\mathbf{F}^{\mathrm{int}}$ and $\mathbf{F}^{\mathrm{ext}}$ are internal and external force in FE subdomain Ω_0^{FE} and they are expressed as

$$\mathbf{F}_{iI}^{\mathrm{int}} = \int_{\Omega_0^{\mathrm{FE}}} \beta^{\mathrm{FE}} N_{I,j}(\mathbf{X}) \mathbf{P}_{ji}(\mathbf{X}) \, \mathrm{d}\Omega_0^{\mathrm{FE}} \tag{59}$$

$$\mathbf{F}_{iI}^{\mathrm{ext}} = \int_{\Omega_0^{\mathrm{FE}}} \beta^{\mathrm{FE}} \rho_0 b_i \, \mathrm{d}\Omega_0^{\mathrm{FE}} + \int_{\Gamma_0^t} \beta^{\mathrm{FE}} \bar{t}_i \, \mathrm{d}\Gamma_0^t \tag{60}$$

and $\mathbf{f}^{\mathrm{int}}$ and $\mathbf{f}^{\mathrm{ext}}$ are internal and external force in particle subdomain Ω_0^{P} and they are expressed as

$$\mathbf{f}_{iI}^{\mathrm{int}} = \int_{\Omega_0^{\mathrm{P}}} \beta^{\mathrm{P}} w_{I,j}(\mathbf{X}) \mathbf{P}_{ji}(\mathbf{X}) \, \mathrm{d}\Omega_0^{\mathrm{P}} \tag{61}$$

$$\mathbf{f}_{iI}^{\mathrm{ext}} = \int_{\Omega_0^{\mathrm{P}}} \beta^{\mathrm{P}} \rho_0 b_i \, \mathrm{d}\Omega_0^{\mathrm{P}} + \int_{\Gamma_0^t} \beta^{\mathrm{P}} \bar{t}_i \, \mathrm{d}\Gamma_0^t \tag{62}$$

Letting $\mathbf{d}$ denote the array of $\mathbf{u}$, the increments in the internal nodal force can be approximated in terms of increments in the nodal displacement by stiffness matrices:

$$\Delta \mathbf{F}_I^{\mathrm{int}} = \sum_J \mathbf{K}_{IJ}^{\mathrm{FE}} \Delta \mathbf{u}_J^{\mathrm{FE}} \quad \text{or} \quad \Delta \mathbf{F}^{\mathrm{int}} = \mathbf{K}^{\mathrm{FE}} \Delta \mathbf{d}^{\mathrm{FE}} \tag{63}$$

$$\Delta \mathbf{f}_I^{\mathrm{int}} = \sum_J \mathbf{K}_{IJ}^{\mathrm{P}} \Delta \mathbf{u}_J^{\mathrm{P}} \quad \text{or} \quad \Delta \mathbf{f}^{\mathrm{int}} = \mathbf{K}^{\mathrm{P}} \Delta \mathbf{d}^{\mathrm{P}} \tag{64}$$

where $\mathbf{K}^{\mathrm{FE}}$ and $\mathbf{K}^{\mathrm{P}}$ are tangent stiffness matrices given by

$$\mathbf{K}^{\mathrm{FE}} = \begin{bmatrix} \mathbf{K}_{11}^{\mathrm{FE}} & \mathbf{K}_{12}^{\mathrm{FE}} & & \\ \mathbf{K}_{21}^{\mathrm{FE}} & \mathbf{K}_{22}^{\mathrm{FE}} & & \\ & & \cdots & \\ & & & \mathbf{K}_{nn}^{\mathrm{FE}} \end{bmatrix}, \quad \mathbf{K}_{IJ}^{\mathrm{FE}} = \frac{\partial \mathbf{F}_I^{\mathrm{int}}}{\partial \mathbf{u}_J^{\mathrm{FE}}} \tag{65}$$

$$\mathbf{K}^{\mathrm{P}} = \begin{bmatrix} \mathbf{K}_{11}^{\mathrm{P}} & \mathbf{K}_{12}^{\mathrm{P}} & & \\ \mathbf{K}_{21}^{\mathrm{P}} & \mathbf{K}_{22}^{\mathrm{P}} & & \\ & & \cdots & \\ & & & \mathbf{K}_{mm}^{\mathrm{P}} \end{bmatrix}, \quad \mathbf{K}_{IJ}^{\mathrm{P}} = \frac{\partial \mathbf{f}_I^{\mathrm{int}}}{\partial \mathbf{u}_J^{\mathrm{P}}} \tag{66}$$

$$\mathbf{d}^{\mathrm{FE}} = \begin{Bmatrix} \mathbf{d}_1^{\mathrm{FE}} \\ \mathbf{d}_2^{\mathrm{FE}} \\ \cdots \\ \mathbf{d}_n^{\mathrm{FE}} \end{Bmatrix}, \quad \mathbf{d}_I^{\mathrm{FE}} = \begin{Bmatrix} u_{xI}^{\mathrm{FE}} \\ u_{yI}^{\mathrm{FE}} \end{Bmatrix}, \quad \mathbf{d}^{\mathrm{P}} = \begin{Bmatrix} \mathbf{d}_1^{\mathrm{P}} \\ \mathbf{d}_2^{\mathrm{P}} \\ \cdots \\ \mathbf{d}_m^{\mathrm{P}} \end{Bmatrix}, \quad \mathbf{d}_I^{\mathrm{P}} = \begin{Bmatrix} u_{xI}^{\mathrm{P}} \\ u_{yI}^{\mathrm{P}} \end{Bmatrix} \tag{67}$$

The system can then be written as

$$\begin{bmatrix} \mathbf{A}_{11} & \mathbf{A}_{12} & \mathbf{L}^{\mathrm{FE}\,\mathrm{T}} \\ \mathbf{A}_{21} & \mathbf{A}_{22} & \mathbf{L}^{\mathrm{P}\,\mathrm{T}} \\ \mathbf{L}^{\mathrm{FE}} & \mathbf{L}^{\mathrm{P}} & 0 \end{bmatrix} \begin{Bmatrix} \Delta \mathbf{d}^{\mathrm{FE}} \\ \Delta \mathbf{d}^{\mathrm{P}} \\ \Delta \bar{\lambda} \end{Bmatrix} = \begin{Bmatrix} -\mathbf{r}^{\mathrm{FE}} \\ -\mathbf{r}^{\mathrm{P}} \\ -\bar{\mathbf{g}} \end{Bmatrix} \tag{68}$$

If we let d_i denote u_{kP} and d_j denote u_{lQ}, the ingredients of Equation (68) can be expressed as

$$\mathbf{r}^{\mathrm{FE}} = \mathbf{F}^{\mathrm{int}} - \mathbf{F}^{\mathrm{ext}} + \boldsymbol{\lambda}^{\mathrm{T}} \mathbf{G}^{\mathrm{FE}} + p \mathbf{g}^{\mathrm{T}} \mathbf{G}^{\mathrm{FE}} \tag{69}$$

$$\mathbf{r}^{\mathrm{P}} = \mathbf{f}^{\mathrm{int}} - \mathbf{f}^{\mathrm{ext}} + \boldsymbol{\lambda}^{\mathrm{T}} \mathbf{G}^{\mathrm{P}} + p \mathbf{g}^{\mathrm{T}} \mathbf{G}^{\mathrm{P}} \tag{70}$$

$$\bar{\mathbf{g}} = \{\bar{g}_{iI}\} = \left\{ \sum_K \Lambda_{IK} g_{iK} \right\} \tag{71}$$

$$\mathbf{A}_{11} = \mathbf{K}^{\mathrm{FE}} + p \mathbf{G}^{\mathrm{FE}\mathrm{T}} \mathbf{G}^{\mathrm{FE}} \tag{72}$$

$$\mathbf{A}_{12} = p \mathbf{G}^{\mathrm{FE}^{\mathrm{T}}} \mathbf{G}^{\mathrm{P}} \tag{73}$$

$$\mathbf{A}_{21} = p \mathbf{G}^{\mathrm{P}^{\mathrm{T}}} \mathbf{G}^{\mathrm{FE}} \tag{74}$$

$$\mathbf{A}_{22} = \mathbf{K}^{\mathrm{P}} + p \mathbf{G}^{\mathrm{P}^{\mathrm{T}}} \mathbf{G}^{\mathrm{P}} \tag{75}$$

$$\lambda_{iI} = \sum_K \Lambda_K(\mathbf{X}_I) \bar{\lambda}_{iK} \tag{76}$$

$$\mathbf{K}^{\mathrm{FE}} = \left[\frac{\partial \mathbf{F}^{\mathrm{int}}}{\partial \mathbf{d}^{\mathrm{FE}}}\right] = \left[\frac{\partial F_{iI}^{\mathrm{int}}}{\partial u_{lQ}^{\mathrm{FE}}}\right] = \left[\int_{\Omega_0^{\mathrm{FE}}} \beta^{\mathrm{FE}} N_{I,j} \overline{C}_{jilk} N_{Q,k} \, \mathrm{d}\Omega_0^{\mathrm{FE}}\right] \tag{77}$$

$$\mathbf{K}^{\mathrm{P}} = \left[\frac{\partial \mathbf{f}^{\mathrm{int}}}{\partial \mathbf{d}^{\mathrm{P}}}\right] = \left[\frac{\partial f_{iI}^{\mathrm{int}}}{\partial u_{lQ}^{\mathrm{P}}}\right] = \left[\int_{\Omega_0^{\mathrm{P}}} \beta^{\mathrm{P}} w_{I,j} \overline{C}_{jilk} w_{Q,k} \, \mathrm{d}\Omega_0^{\mathrm{P}}\right] \tag{78}$$

$$\mathbf{L}^{\mathrm{FE}} = \left[\sum_L \Lambda_{IL} \frac{\partial \mathbf{g}_L}{\partial d_i^{\mathrm{FE}}}\right] = \left[\sum_L \Lambda_{IL} \frac{\partial g_{jL}}{\partial d_i^{\mathrm{FE}}}\right] = \left[\sum_L \Lambda_{IL} \frac{\partial g_L}{\partial u_{kP}^{\mathrm{FE}}}\right] = \left[\sum_L \Lambda_{IL} N_{PI} \delta_{jk}\right] \tag{79}$$

$$\mathbf{L}^{\mathrm{P}} = \left[\sum_L \Lambda_{IL} \frac{\partial \mathbf{g}_L}{\partial d_i^{\mathrm{P}}}\right] = \left[\sum_L \Lambda_{IL} \frac{\partial g_{jL}}{\partial d_i^{\mathrm{P}}}\right] = \left[\sum_L \Lambda_{IL} \frac{\partial g_L}{\partial u_{kP}^{\mathrm{P}}}\right] = \left[-\sum_L \Lambda_{IL} w_{PI} \delta_{jk}\right] \tag{80}$$

$$\begin{aligned} \mathbf{G}^{\mathrm{FE}} &= \left[\frac{\partial \mathbf{g}_I}{\partial d_i^{\mathrm{FE}}}\right] = \left[\frac{\partial g_{jI}}{\partial u_{kP}^{\mathrm{FE}}}\right] = [N_{PI} \delta_{jk}] \\ \mathbf{G}^{\mathrm{P}} &= \left[\frac{\partial \mathbf{g}_I}{\partial d_i^{\mathrm{P}}}\right] = \left[\frac{\partial g_{jI}}{\partial u_{kP}^{\mathrm{P}}}\right] = [-w_{PI} \delta_{jk}] \end{aligned} \tag{81}$$

5.3.3. Explicit time integration. In dynamics, the Lagrangian of the system is

$$L = W^{\mathrm{kin}} - W^{\mathrm{int}} + W^{\mathrm{ext}} \tag{82}$$

where $W^{\mathrm{kin}} = \sum_I m_I \frac{1}{2} \dot{d}_I^2$ is kinetic energy.

Therefore, the Lagrangian for the coupling model is

$$L = L^{\mathrm{FE}} + L^{\mathrm{P}} = \beta^{\mathrm{FE}} W_{\mathrm{FE}}^{\mathrm{kin}} - \beta^{\mathrm{FE}} W_{\mathrm{FE}}^{\mathrm{int}} + \beta^{\mathrm{FE}} W_{\mathrm{FE}}^{\mathrm{ext}} + \beta^{\mathrm{P}} W_{\mathrm{P}}^{\mathrm{kin}} - \beta^{\mathrm{P}} W_{\mathrm{P}}^{\mathrm{int}} + \beta^{\mathrm{P}} W_{\mathrm{P}}^{\mathrm{ext}} \tag{83}$$

The Lagrangian for augmented Lagrangian method is

$$L^{\mathrm{AL}} = L + \boldsymbol{\lambda}^{\mathrm{T}} \mathbf{g} + \tfrac{1}{2} \, p \mathbf{g}^{\mathrm{T}} \mathbf{g} \tag{84}$$

In Lagrangian mechanics the equations of motion are written as

$$\frac{\mathrm{d}}{\mathrm{d}t}\left(\frac{\partial L}{\partial \dot{d}}\right) = \frac{\partial L}{\partial d} \tag{85}$$

Then, we obtain the equations of motion by substituting Equation (84) into Equation (85):

$$\overline{\mathbf{M}} \ddot{\mathbf{u}}^{\mathrm{FE}} + \mathbf{F}^{\mathrm{int}} - \mathbf{F}^{\mathrm{ext}} - \mathbf{F}^{C} = 0 \tag{86}$$

$$\overline{\mathbf{m}} \ddot{\mathbf{u}}^{\mathrm{P}} + \mathbf{f}^{\mathrm{int}} - \mathbf{f}^{\mathrm{ext}} - \mathbf{f}^{C} = 0 \tag{87}$$

where

$$\overline{M}_{IJ} = \int_{\Omega_0^{\mathrm{FE}}} \beta^{\mathrm{FE}} \rho_0 N_I(X) N_J(X) \, \mathrm{d}\Omega_0^{\mathrm{FE}} \tag{88}$$

$$\overline{m}_{IJ} = \int_{\Omega_0^{\mathrm{P}}} \beta^{\mathrm{P}} \rho_0 w_I(X) w_J(X) \, \mathrm{d}\Omega_0^{\mathrm{P}} \tag{89}$$

the internal and external forces are define as before. $\mathbf{F}^C$ and $\mathbf{f}^C$ are extra forces from the constraints

$$\mathbf{F}^C = \boldsymbol{\lambda}^{\mathrm{T}} \frac{\partial \mathbf{g}}{\partial \mathbf{u}^{\mathrm{FE}}} + p\mathbf{g}^{\mathrm{T}} \frac{\partial \mathbf{g}}{\partial \mathbf{u}^{\mathrm{FE}}} = \boldsymbol{\lambda}^{\mathrm{T}} \mathbf{G}^{\mathrm{FE}} + p\mathbf{g}^{\mathrm{T}} \mathbf{G}^{\mathrm{FE}} \tag{90}$$

$$\mathbf{f}^C = \boldsymbol{\lambda}^{\mathrm{T}} \frac{\partial \mathbf{g}}{\partial \mathbf{u}^{\mathrm{P}}} + p\mathbf{g}^{\mathrm{T}} \frac{\partial \mathbf{g}}{\partial \mathbf{u}^{\mathrm{P}}} = \boldsymbol{\lambda}^{\mathrm{T}} \mathbf{G}^{\mathrm{P}} + p\mathbf{g}^{\mathrm{T}} \mathbf{G}^{\mathrm{P}} \tag{91}$$

Equations (87) and (86) can be written in a general form:

$$\mathbf{M}\ddot{\mathbf{d}} = \mathbf{f}^{\mathrm{ext}} - \mathbf{f}^{\mathrm{int}} + \mathbf{f}^C \tag{92}$$

In time step $n+1$, we first obtain the *trial* velocities by

$$\bar{\mathbf{v}} = \mathbf{v}_{(n)} + \mathbf{M}^{-1}\Delta t \left(\mathbf{f}^{\mathrm{ext}} - \mathbf{f}^{\mathrm{int}} + p\mathbf{g}^{\mathrm{T}}\mathbf{G}\right) \tag{93}$$

The trial velocities need to be corrected by applying the constraint equations, which are written in time derivative form

$$\dot{\mathbf{g}}_I = \mathbf{v}_I^{\mathrm{FE}} - \mathbf{v}_I^{\mathrm{P}} = \sum_J N_{JI}\mathbf{v}_J^{\mathrm{FE}} - \sum_J w_{JI}\mathbf{v}_J^{\mathrm{P}} = 0 \tag{94}$$

where the velocities are the values at time step $n+1$ and given by

$$\begin{aligned} \mathbf{v}_{(n+1)} &= \mathbf{v}_{(n)} + \mathbf{M}^{-1}\Delta t \left(\mathbf{f}^{\mathrm{ext}} - \mathbf{f}^{\mathrm{int}} + \boldsymbol{\lambda}^{\mathrm{T}}\mathbf{G} + p\mathbf{g}^{\mathrm{T}}\mathbf{G}\right) \\ &= \bar{\mathbf{v}} + \mathbf{M}^{-1}\Delta t \boldsymbol{\lambda}^{\mathrm{T}}\mathbf{G} \end{aligned} \tag{95}$$

Substituting Equation (95) into Equation (94), the Lagrange multiplier can be obtained by solving the following equations:

$$\left(\sum_J \frac{\Delta t}{M_J} w_{JI}\mathbf{G}_{LJ}^{\mathrm{P}} - \sum_K \frac{\Delta t}{M_K} N_{KI}\mathbf{G}_{LK}^{\mathrm{FE}}\right)\boldsymbol{\lambda}_L = \left(\sum_J N_{JI}\bar{\mathbf{v}}_J^{\mathrm{FE}} - \sum_K w_{KI}\bar{\mathbf{v}}_K^{\mathrm{P}}\right) \tag{96}$$

$$\boldsymbol{\lambda}_L = \begin{Bmatrix} \lambda_{xL} \\ \lambda_{yL} \end{Bmatrix} \quad \bar{\mathbf{v}}_J^{\mathrm{FE}} = \begin{Bmatrix} \bar{v}_{xJ}^{\mathrm{FE}} \\ \bar{v}_{yJ}^{\mathrm{FE}} \end{Bmatrix} \quad \bar{\mathbf{v}}_K^{\mathrm{P}} = \begin{Bmatrix} \bar{v}_{xK}^{\mathrm{P}} \\ \bar{v}_{yK}^{\mathrm{P}} \end{Bmatrix} \tag{97}$$

The Lagrange multipliers, which are set on the positions of discrete atoms, are treated as unknown variables in the dynamic algorithm. The algorithm is given in Table I.

Table I. Explicit algorithm for dynamics with coupling method.

1. initial conditions and initialization: $t = 0$ and compute $\mathbf{M}$;
2. get $\mathbf{f}^{\mathrm{int}}$, $\mathbf{f}^{\mathrm{ext}}$ and $\mathbf{f}^C$ which is from Equation (92);
3. compute trial velocities from Equation (93);
4. compute the unknown of Lagrange multipliers $\Delta\lambda$ from Equation (96);
5. update velocities from Equation (95);
6. apply boundary conditions;
7. output; if simulation does not complete, go to 2

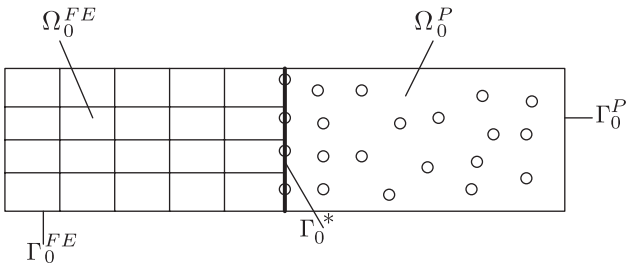

Figure 6. Coupling of particle and finite elements.

5.4. *Compatibility coupling: coupling with Lagrange multipliers*

A coupling approach where no ramp functions are needed was first proposed by Hegen [12]. Rabczuk and Belytschko [13] used this approach to couple EFG nodes and FEs to model the bond behaviour in reinforced concrete beams in statics. In this method, relative displacements between the particles and the elements are allowed. Xiao [45] developed an explicit method based on Lagrange multipliers (similar to the approach of Hegen [12]) which is a simplified version of the bridging domain coupling. He called this method edge-to-edge coupling. The main difference is that the FE and particle domain do not overlap, which simplifies the method enormously. However, for wave propagation problems, the bridging domain coupling is more accurate. We will review the coupling via Lagrange multipliers as in Reference [13] and extend it to dynamics.

For the static case, the potential to be minimized is

$$W = W^{\text{int}} - W^{\text{ext}} + \boldsymbol{\lambda}^{\text{T}}\mathbf{g} \tag{98}$$

where W^{int} is the internal and W^{ext} is the external energy. The last term on the RHS are the constraints. In the dynamic case, an inertia term is added. The Lagrange multipliers are denoted by $\boldsymbol{\lambda}$ and $\mathbf{g} = \mathbf{u}^{\text{FE}} - \mathbf{u}^{\text{P}}$ is the gap of the particle and the FE domain along the common boundary as illustrated in Figure 6. The Lagrange multipliers are located at the particle positions and are

$$\mathbf{g}_h = \sum_{J=1}^{N} N_J^{\text{FE}}(\mathbf{X},t)\mathbf{u}_J^{\text{FE}} - \sum_{J\in S} N_J^{\text{P}}(\mathbf{X},t)\mathbf{u}_J^{\text{P}} \tag{99}$$

The Lagrange multiplier estimates are placed at the particle position and FE shape functions are used to discretize the Lagrange multiplier field $\delta\boldsymbol{\lambda}$:

$$\delta\boldsymbol{\lambda}_h^{\text{P}}(\mathbf{X},t) = \sum_{J=1}^{N} N_J^{\text{FE}}(\mathbf{X},t)\delta\boldsymbol{\Lambda}_J(t) \tag{100}$$

Note that for the interpolation in Equation (100), the position of the Lagrange multipliers in the local element co-ordinate system has to be known. The test and trial functions are

$$\delta\mathbf{u}_h(\mathbf{X},t) = \sum_{J=1}^{N} N_J^{\text{FE}}(\mathbf{X},t)\delta\mathbf{u}_J^{\text{FE}}(t) + \sum_{J\in\mathscr{S}} N_J^{\text{P}}(\mathbf{X},t)\delta\mathbf{u}_J^{\text{P}}(t) \tag{101}$$

$$\mathbf{u}_h(\mathbf{X},t) = \sum_{J=1}^{N} N_J^{\text{FE}}(\mathbf{X},t)\mathbf{u}_J^{\text{FE}}(t) + \sum_{J\in\mathscr{S}} N_J^{\text{P}}(\mathbf{X},t)\mathbf{u}_J^{\text{P}}(t) \tag{102}$$

and

$$N^{\mathrm{FE}}(\mathbf{X},t)=0 \quad \forall \mathbf{X}\in\Omega_0^{\mathrm{P}}$$
$$N^{\mathrm{P}}(\mathbf{X},t)=0 \quad \forall \mathbf{X}\in\Omega_0^{\mathrm{FE}} \tag{103}$$

where $\mathscr{S}$ is the set of nodes in the particle model.

Minimizing Equation (98) with respect to $\mathbf{u}$ and $\boldsymbol{\lambda}$ leads to the following equations:

$$\begin{aligned}\frac{\partial W}{\partial \mathbf{u}}&=\frac{\partial W^{\mathrm{int}}}{\partial \mathbf{u}}-\frac{\partial W^{\mathrm{ext}}}{\partial \mathbf{u}}+\boldsymbol{\lambda}\frac{\partial \mathbf{g}}{\partial \mathbf{u}}=\mathbf{f}^{\mathrm{int}}-\mathbf{f}^{\mathrm{ext}}+\boldsymbol{\lambda}\frac{\partial \mathbf{g}}{\partial \mathbf{u}}=0\\ \frac{\partial W}{\partial \boldsymbol{\lambda}}&=\mathbf{g}=0\end{aligned} \tag{104}$$

The derivatives of W^{int} and W^{ext} with respect to $\mathbf{u}$ are the internal and external forces, respectively:

$$\mathbf{f}^{\mathrm{int}}=\int_{\Omega_0^{\mathrm{P}}\cup\Omega_0^{\mathrm{FE}}}(\nabla_0\otimes\delta\mathbf{u})^{\mathrm{T}}:\mathbf{P}\,\mathrm{d}\Omega_0 \tag{105}$$

$$\mathbf{f}^{\mathrm{ext}}=\int_{\Omega_0^{\mathrm{P}}\cup\Omega_0^{\mathrm{FE}}}\delta\mathbf{u}\cdot\mathbf{b}\,\mathrm{d}\Omega_0+\int_{\Gamma_0^{\mathrm{P},t}\cup\Gamma_0^{\mathrm{FE},t}}\delta\mathbf{u}\cdot\bar{\mathbf{t}}_0\,\mathrm{d}\Gamma_0 \tag{106}$$

The additional forces $\boldsymbol{\lambda}(\partial\mathbf{g}/\partial\mathbf{u})$ are linear combinations of the Lagrange multipliers. To obtain the discrete system of non-linear equations we will do a linearization as described, e.g. in Reference [3]. Therefore, we take a Taylor series expansion of Equation (104) neglecting any higher-order terms:

$$\begin{aligned}\mathbf{f}^{\mathrm{int}}-\mathbf{f}^{\mathrm{ext}}+\boldsymbol{\lambda}\frac{\partial \mathbf{g}}{\partial \mathbf{u}}+\frac{\partial \mathbf{f}^{\mathrm{int}}}{\partial \mathbf{u}}\Delta\mathbf{u}-\frac{\partial \mathbf{f}^{\mathrm{ext}}}{\partial \mathbf{u}}\Delta\mathbf{u}+\frac{\partial \mathbf{g}}{\partial \mathbf{u}}\Delta\boldsymbol{\lambda}+\boldsymbol{\lambda}\frac{\partial^2\mathbf{g}}{\partial\mathbf{u}\partial\mathbf{u}}\Delta\mathbf{u}&=0\\ \mathbf{u}+\frac{\partial \mathbf{g}}{\partial \mathbf{u}}\Delta\mathbf{u}&=0\end{aligned} \tag{107}$$

Substituting the test and trial functions, Equations (100)–(102) into (107) we finally obtain the following system of equations:

$$\begin{bmatrix}\mathbf{K}^{\mathrm{FE}}+\boldsymbol{\lambda}\dfrac{\partial^2\mathbf{g}}{\partial\mathbf{u}\partial\mathbf{u}} & 0 & (\mathbf{K}^{\mathrm{FE-FE}})^{\mathrm{T}}\\ 0 & \mathbf{K}^{\mathrm{P}}+\boldsymbol{\lambda}\dfrac{\partial^2\mathbf{g}}{\partial\mathbf{u}\partial\mathbf{u}} & (\mathbf{K}^{\mathrm{FE-P}})^{\mathrm{T}}\\ \mathbf{K}^{\mathrm{FE-FE}} & (\mathbf{K}^{\mathrm{FE-P}})^{\mathrm{T}} & 0\end{bmatrix}\cdot\begin{bmatrix}\Delta\mathbf{u}_J^{\mathrm{FE}}\\ \Delta\mathbf{u}_J^{\mathrm{P}}\\ \Delta\boldsymbol{\Lambda}\end{bmatrix}$$
$$=\begin{bmatrix}\mathbf{f}^{\mathrm{ext,FE}}-\mathbf{f}^{\mathrm{int,FE}}-\boldsymbol{\lambda}^{\mathrm{T}}\mathbf{K}^{\mathrm{FE-FE}}\\ \mathbf{f}^{\mathrm{ext,P}}-\mathbf{f}^{\mathrm{int,P}}-\boldsymbol{\lambda}^{\mathrm{T}}\mathbf{K}^{\mathrm{FE-P}}\\ -\mathbf{g}\end{bmatrix} \tag{108}$$

where $\mathbf{K}^{\mathrm{FE-FE}}$ and $\mathbf{K}^{\mathrm{FE-P}}$ denotes the derivatives of $\mathbf{g}$ with respect to $\mathbf{u}$ for the FE ($\mathbf{u}^{\mathrm{FE}}$) and particle domain ($\mathbf{u}^{\mathrm{P}}$), respectively, and $\mathbf{K}^{\mathrm{FE}}$ and $\mathbf{K}^{\mathrm{P}}$ are the derivatives of the internal

and external forces with respect to $\mathbf{u}$. Since neither $\mathbf{b}$ nor the traction boundary conditions $\bar{\mathbf{t}}$ depend on $\mathbf{u}$, the derivatives on $\mathbf{f}^{\text{ext}}$ exist only for the cohesive model. Finally, we can give the matrices:

$$\begin{aligned}
\mathbf{K}^{\text{FE}-\text{FE}} &= \int_{\Gamma_0^*} (\mathbf{N}^{\text{FE}})^{\text{T}} \cdot \mathbf{N}^{\text{FE}} \, \mathrm{d}\Gamma_0 \\
\mathbf{K}^{\text{FE}-\text{P}} &= -\int_{\Gamma_0^*} (\mathbf{N}^{\text{FE}})^{\text{T}} \cdot \mathbf{N}^{\text{P}} \, \mathrm{d}\Gamma_0 \\
\mathbf{K}^{\text{P}} &= \int_{\Omega_0^{\text{P}}} (\mathbf{B}^{\text{P}})^{\text{T}} \mathbf{C} \mathbf{B}^{\text{P}} \, \mathrm{d}\Omega_0 \\
\mathbf{K}^{\text{FE}} &= \int_{\Omega_0^{\text{FE}}} (\mathbf{B}^{\text{FE}})^{\text{T}} \mathbf{C} \mathbf{B}^{\text{FE}} \, \mathrm{d}\Omega_0
\end{aligned} \tag{109}$$

and the vectors for internal and external forces

$$\begin{aligned}
\mathbf{f}^{\text{ext,FE}} &= \int_{\Omega_0^{\text{FE}}} (\mathbf{N}^{\text{FE}})^{\text{T}} \mathbf{b} \, \mathrm{d}\Omega_0 + \int_{\Gamma_0^{\text{FE},t}} (\mathbf{N}^{\text{FE}})^{\text{T}} \bar{\mathbf{t}}_0 \, \mathrm{d}\Gamma_0 \\
\mathbf{f}^{\text{ext,P}} &= \int_{\Omega_0^{\text{P}}} (\mathbf{N}^{\text{P}})^{\text{T}} \mathbf{b} \, \mathrm{d}\Omega_0 + \int_{\Gamma_0^{\text{P},t}} (\mathbf{N}^{\text{P}})^{\text{T}} \bar{\mathbf{t}}_0 \, \mathrm{d}\Gamma_0 \\
\mathbf{f}^{\text{int,FE}} &= \int_{\Omega_0^{\text{FE}}} (\mathbf{B}^{\text{FE}})^{\text{T}} \cdot \mathbf{P} \, \mathrm{d}\Omega_0 \\
\mathbf{f}^{\text{int,P}} &= \int_{\Omega_0^{\text{P}}} (\mathbf{B}^{\text{P}})^{\text{T}} \cdot \mathbf{P} \, \mathrm{d}\Omega_0
\end{aligned} \tag{110}$$

For dynamics, let us define the problem for every domain separately: Find $\mathbf{u}^i \in H^1(\Omega^i)$, $i = \text{FE}$ or P and $\boldsymbol{\lambda} \in H^0(\Gamma^*)$ so that

$$\begin{aligned}
&\int_{\Omega_0^{\text{FE}}} \varrho_0^{\text{FE}} \delta\mathbf{u}^{\text{FE}} \cdot \ddot{\mathbf{u}}^{\text{FE}} \, \mathrm{d}\Omega_0 + \int_{\Omega_0^{\text{FE}}} \nabla\delta\mathbf{u}^{\text{FE}} : \mathbf{P}^{\text{FE}} \, \mathrm{d}\Omega_0 - \int_{\Omega_0^{\text{FE}}} \delta\mathbf{u}^{\text{FE}} \cdot \mathbf{b}^{\text{FE}} \, \mathrm{d}\Omega_0 \\
&- \int_{\Gamma_0^{1t}} \delta\mathbf{u}^{\text{FE}} \cdot \bar{\mathbf{t}}^{\text{FE}} \, \mathrm{d}\Gamma - \int_{\Gamma_*} \delta\boldsymbol{\lambda} \cdot \mathbf{u}^{\text{FE}} \, \mathrm{d}\Gamma - \int_{\Gamma_*} \delta\mathbf{u}^{\text{FE}} \cdot \boldsymbol{\lambda} \, \mathrm{d}\Gamma = 0
\end{aligned} \tag{111}$$

$$\begin{aligned}
&\int_{\Omega_0^{p}} \varrho_0^{\text{P}} \delta\mathbf{u}^{\text{P}} \cdot \ddot{\mathbf{u}}^{\text{P}} \, \mathrm{d}\Omega_0 + \int_{\Omega_0^{\text{P}}} \nabla\delta\mathbf{u}^{\text{P}} : \mathbf{P}^{\text{P}} \, \mathrm{d}\Omega_0 - \int_{\Omega_0^{\text{P}}} \delta\mathbf{u}^{\text{P}} \cdot \mathbf{b}^{\text{P}} \, \mathrm{d}\Omega_0 \\
&- \int_{\Gamma_0^{Pt}} \delta\mathbf{u}^{\text{P}} \cdot \bar{\mathbf{t}}^{\text{P}} \, \mathrm{d}\Gamma + \int_{\Gamma_*} \delta\boldsymbol{\lambda} \cdot \mathbf{u}^{\text{P}} \, \mathrm{d}\Gamma + \int_{\Gamma_*} \delta\mathbf{u}^{\text{P}} \cdot \boldsymbol{\lambda} \, \mathrm{d}\Gamma = 0
\end{aligned} \tag{112}$$

for all $\delta\mathbf{u}^i \in H^1(\Omega^i)$, $i = \text{FE}$ or P and $\delta\boldsymbol{\lambda} \in H^0(\Gamma_*)$ where the superscript i indicates the corresponding domain (Ω^{FE} and Ω^{P}), respectively. Note that for the dynamic scheme, the displacements $\mathbf{u}^i$, $i = \text{FE}$ or P in the fifth term on the LHS of Equations (111) and (112) are replaced

by their accelerations $\ddot{\mathbf{u}}^i$, $i = \text{FE}$ or P to obtain the discrete equations. The test and trial functions in a Bubnov–Galerkin method are approximated via the same shape function

$$\delta \mathbf{u}_h^i(\mathbf{X}, t) = \sum_{J=1}^{N} N_J^i(\mathbf{X}, t) \delta \mathbf{u}_J^i(t) \tag{113}$$

$$\mathbf{u}_h^i(\mathbf{X}, t) = \sum_{J=1}^{N} N_J^i(\mathbf{X}, t) \mathbf{u}_J^i(t) \tag{114}$$

where the superscript i indicates the corresponding domain (Ω^{FE} and Ω^{P}). The Lagrange multipliers are approximated to

$$\boldsymbol{\lambda}_h^i = \sum_{J=1}^{N} \Lambda_J \boldsymbol{\lambda}_J^i \tag{115}$$

$$\delta \boldsymbol{\lambda}_h^i = \sum_{J=1}^{N} \Lambda_J \delta \boldsymbol{\lambda}_J^i \tag{116}$$

where for the Λ the FE shape functions are chosen. Finally, we obtain with the traction and displacement continuity the equation of motion

$$\sum_{J=1} \mathbf{m}_{IJ} \ddot{\mathbf{u}}_J = \mathbf{f}_I^{\text{ext}} - \mathbf{f}_I^{\text{int}} \tag{117}$$

with

$$\mathbf{m} = \begin{bmatrix} \mathbf{m}^{\text{FE}} & 0 & -\mathbf{G}^{\text{FE}} \\ 0 & \mathbf{m}^{\text{P}} & \mathbf{G}^{\text{P}} \\ -\mathbf{G}^{\text{FE}} & \mathbf{G}^{\text{P}} & 0 \end{bmatrix} \tag{118}$$

$$\mathbf{u} = \begin{bmatrix} \mathbf{u}^{\text{FE}} \\ \mathbf{u}^{\text{P}} \\ \boldsymbol{\lambda} \end{bmatrix} \tag{119}$$

$$\mathbf{F} = \begin{bmatrix} \mathbf{f}^{\text{int},1} - \mathbf{f}^{\text{ext},1} \\ \mathbf{f}^{\text{int},2} - \mathbf{f}^{\text{ext},2} \\ -\mathbf{g} \end{bmatrix} \tag{120}$$

and

$$\mathbf{m}_{IJ}^i = \sum_I \int_{\Omega_0^i} \varrho_0^i N_I^i N_J^i \, \mathrm{d}\Omega_0^i, \quad i = \text{FE or P} \tag{121}$$

$$\mathbf{G}_{IJ}^i = \int_{\Gamma_0^u} N_I^i \boldsymbol{\Lambda}_J \, \mathrm{d}\Gamma_0^i \tag{122}$$

$$\mathbf{f}_I^{\text{int},i} = \int_{\Omega_0^i} \nabla N_I^i \cdot \mathbf{P}^i \, \mathrm{d}\Omega_0^i, \quad i = \text{FE or P} \tag{123}$$

$$\mathbf{f}_I^{\text{ext},i} = \int_{\Gamma_0^i} \varrho_0^i N_I^i \mathbf{b}^i + N_I^i \bar{\mathbf{t}}^i \, \mathrm{d}\Gamma_0^i, \quad i = \text{FE or P} \tag{124}$$

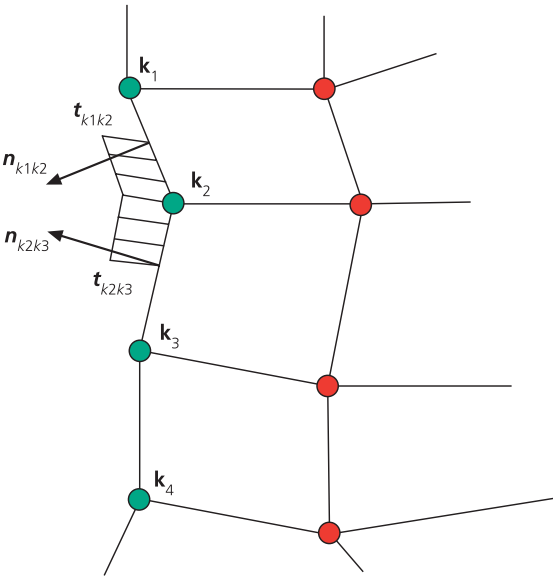

Figure 7. Hybrid FE–particle coupling.

where the superscript i designates either the particle or FE domain. Note that we used here a consistent mass matrix. When the mass is lumped, a scheme as explained in detail in Table I can be used.

5.5. *Hybrid approximation*

The principle of the hybrid (FE–mesh-free method) coupling is explained in Figure 7. For the particle approximation, the FE domain is included in the sums of the mesh-free approximation:

$$u_I^h(\mathbf{X}) = \sum_J u_J N(\mathbf{X}_J - \mathbf{X}_I, h_0) + \int_{\Omega^{\mathrm{FE}\cap\mathrm{P}}} u^{\mathrm{FE}} N(\mathbf{X}^{\mathrm{FE}} - \mathbf{X}_I, h_0)\,\mathrm{d}\Omega_0 \tag{125}$$

$$\nabla u_I^h(\mathbf{X}) = \sum_J u_J \nabla N(\mathbf{X}_J - \mathbf{X}_I, h_0) + \int_{\Omega^{\mathrm{FE}\cap\mathrm{P}}} u^{\mathrm{FE}} \nabla N(\mathbf{X}^{\mathrm{FE}} - \mathbf{X}_I, h_0)\,\mathrm{d}\Omega_0 \tag{126}$$

where the first term on the RHS of Equations (125) and (126) is the usual discrete mesh-free approximation and the second term is the enhancement in the hybrid domain $\Omega^{\mathrm{FE}\cap\mathrm{P}}$. Applying this procedure to the typical SPH-form of the momentum equation, we obtain

$$\begin{aligned}\ddot{\mathbf{u}}_I(\mathbf{X}) = &-\frac{1}{\varrho_0}\sum_J (\mathbf{P}(\mathbf{X}_J) + \mathbf{P}(\mathbf{X}_I)) \cdot \nabla N(\mathbf{X}_J - \mathbf{X}_I, h_0) \\ &-\frac{1}{\varrho_0}\int_{\Omega^{\mathrm{FE}\cap\mathrm{P}}} (\mathbf{P}(\mathbf{X}^{\mathrm{FE}}) + \mathbf{P}(\mathbf{X}_I)) \cdot \nabla N(\mathbf{X}_J - \mathbf{X}_I, h_0)\,\mathrm{d}\Omega_0\end{aligned} \tag{127}$$

The incremental deformation gradient $\nabla \mathbf{u}(\mathbf{X}_I)$ is computed by the same technique:

$$\nabla \mathbf{u}(\mathbf{X}_I) = -\sum_J (\mathbf{u}(\mathbf{X}_J) - \mathbf{u}(\mathbf{X}_I)) \otimes \nabla N(\mathbf{X}_J - \mathbf{X}_I, h_0) - \int_{\Omega^{\mathrm{FE}\cap \mathrm{P}}} (\mathbf{u}(\mathbf{X}^{\mathrm{FE}}) - \mathbf{u}(\mathbf{X}_I)) \otimes \nabla N(\mathbf{X}^{\mathrm{FE}} - \mathbf{X}_I, h_0)\, \mathrm{d}\Omega_0 \tag{128}$$

Especially, the possibility to compute the deformation gradient is the large advantage of the hybrid coupling versus other *strong-form* couplings developed by Johnson [4] and Attaway *et al.* [2]. Since the particle sums remain symmetric, it is guaranteed that the deformation gradient is computed correctly. Another advantage is that the approximation is independent of the relation between the particle distance and the FE length. Since no transition elements are needed for this coupling, adaptivity can be incorporated quite easily as proposed by Sauer [20].

The approach shown above can be easily extended to improved SPH approximation schemes, as normalized SPH [20] or stress point integration versions of the EFG method. For the FEs, the integrals in the hybrid domain $\Omega^{\mathrm{FE}\cap \mathrm{P}}$ can be evaluated by Gauss quadrature. However, as shown by Sauer [20], using (in local co-ordinates) equally spaced integration points in approximately the same density as the SPH particles gave the most accurate results for most examples tested. For a two-dimensional quadrilateral element, a function in the discrete form can be computed as

$$\int_{\Omega^{\mathrm{FE}\cap \mathrm{P}}} u(x,y)N(x,y)\, \mathrm{d}\Omega_0 = \sum_J \sum_{i=1}^{m} \sum_{j=1}^{n} w_i w_j u(\xi_i, \eta_j) N(x_i, y_i) |\mathbf{J}(\xi_i, \eta_j)| \tag{129}$$

and its spatial derivative as

$$\int_{\Omega^{\mathrm{FE}\cap \mathrm{P}}} u(x,y)\nabla N(x,y)\, \mathrm{d}\Omega_0 = \sum_J \sum_{i=1}^{m} \sum_{j=1}^{n} w_i w_j u(\xi_i, \eta_j) \nabla N(x_i, y_i) |\mathbf{J}(\xi_i, \eta_j)| \tag{130}$$

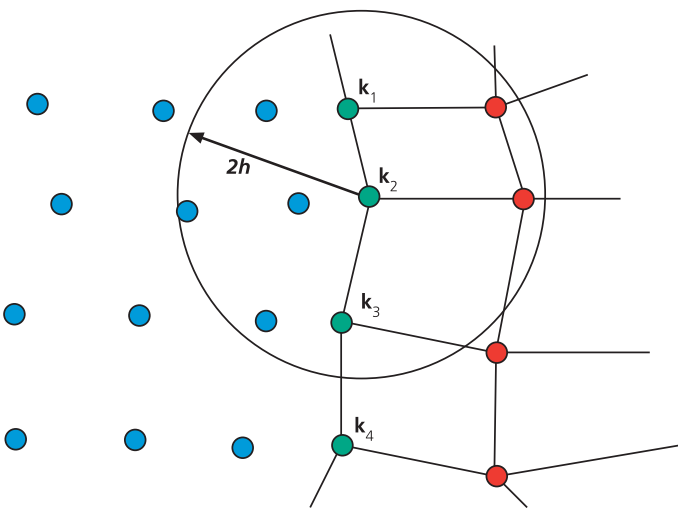

Figure 8. Force transmission on the element nodes in the hybrid domain.

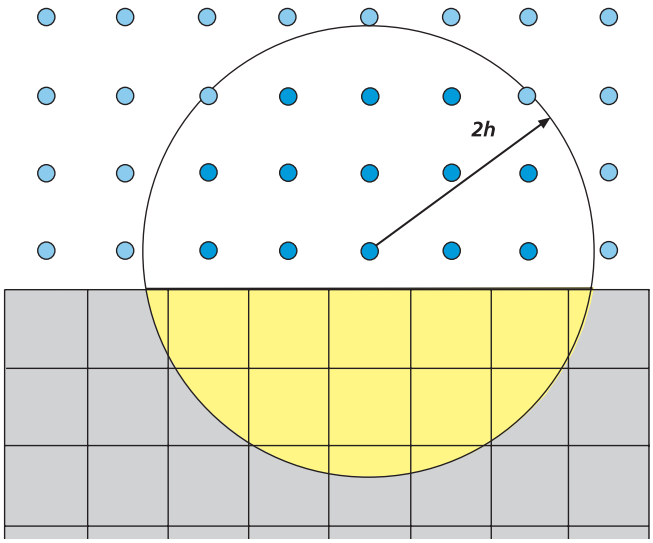

Figure 9. Edge-to-edge coupling using the visibility criterion.

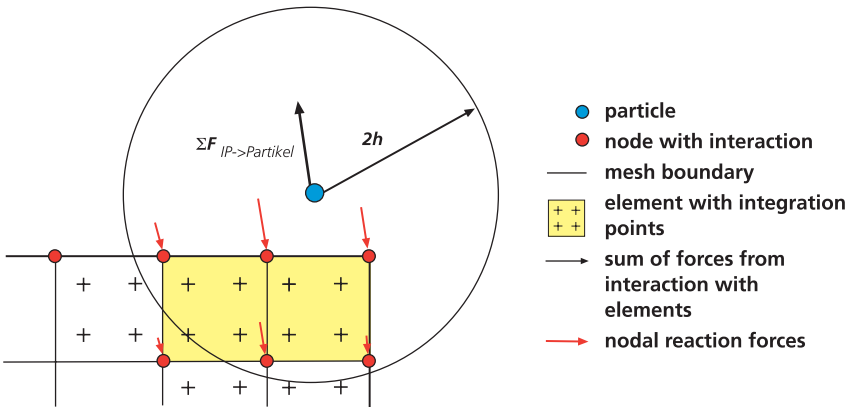

Figure 10. Force transmission via interpolation.

where w_i and w_j are the weights in the corresponding direction ξ_i and η_j, respectively, ξ_i and η_j are local co-ordinates, m is the number of integration points in ξ-direction, n the number of integration points in η-direction and $\mathbf{J}$ designates the Jacobian matrix.

Crucial is how to apply the forces on the element nodes in the hybrid domain. Sauer [20] proposed two different techniques. One possibility is to impose the forces from the particle domain on the element–particle boundary as shown in Figure 8. The stresses for boundary

particle k_2 (see Figure 8) are then

$$\mathbf{P}_{k_2} = \frac{\sum_J \mathbf{P}(\mathbf{X}_J) N(\mathbf{X}_J - \mathbf{X}_I, h_0)}{\sum_J N(\mathbf{X}_J - \mathbf{X}_I, h_0)} \tag{131}$$

The traction on the adjacent element sides according to Figure 8 can then be expressed as

$$\mathbf{t}_{k_1 k_2} = \mathbf{n}_{k_1 k_2} \cdot \mathbf{P}_{k_2} \tag{132}$$

$$\mathbf{t}_{k_2 k_3} = \mathbf{n}_{k_2 k_3} \cdot \mathbf{P}_{k_2} \tag{133}$$

and the internal forces for node 2:

$$\mathbf{F}_2 = \frac{l_{12}}{2} \mathbf{t}_{k_1 k_2} + \frac{l_{23}}{2} \mathbf{t}_{k_2 k_3} \tag{134}$$

where l_{12} denotes the length of the side from node k_1 to node k_2 and l_{23} denotes the length of the side from node k_2 to node k_3. Care has to be taken at edges as shown in Figure 9. Therefore, a visibility criterion is incorporated, so that only particles contribute to the sums, which can be seen by the corresponding element boundary node. In the following, this coupling will be denoted as *HA–S* coupling.

Another possibility to apply the forces from the particles to the FEs, is shown in Figure 10. The advantage of this methods is its robustness since it is not sensitive with respect to changes in the element topology, and therefore easy to use in three dimensions. The internal force can be calculated as

$$\mathbf{F} = -w_{\mathrm{GP}} \det \mathbf{J}_{\mathrm{GP}} (\mathbf{P}(\mathbf{X}_{\mathrm{GP}}^{\mathrm{FE}}) + \mathbf{P}(\mathbf{X}_I)) \cdot N(\mathbf{X}^{\mathrm{FE}} - \mathbf{X}_I, h_0) \tag{135}$$

In the following, this coupling approach will be denoted as *HA–F* coupling. We used the central difference time integration.

6. NUMERICAL EXAMPLES

6.1. Static examples

6.1.1. Timoshenko beam problem. We will test the different methods for a cantilever beam of length L and height D with a traction of P at the free end as shown in Figure 11. The

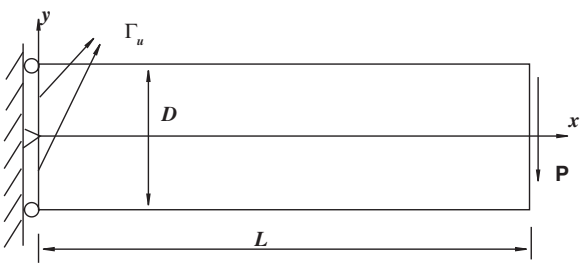

Figure 11. Timoshenko elastic beam.

model is considered to be of unit thickness and in a state of plane stress. The exact solution of this problem has been given by Timoshenko and Goodier [46]:

$$u_x = -\frac{P}{6EI}\left[(6L-3x)x + (2+v)\left(y^2 - \frac{D^2}{4}\right)\right]$$

$$u_y = \frac{P}{6EI}\left[3vy^2(L-x) + (4+5v)\frac{Dx^2}{4} + (3L-x)x^2\right]$$

where the moment of inertia $I = D^3/12$ and the other parameters used here are

$$E = 3 \times 10^7, \quad v = 0.3, \quad D = 12, \quad L = 48, \quad P = 1000$$

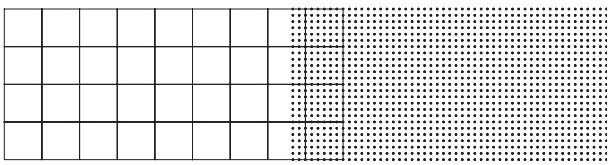

Figure 12. Bridging domain coupling: finite element and particle arrangement.

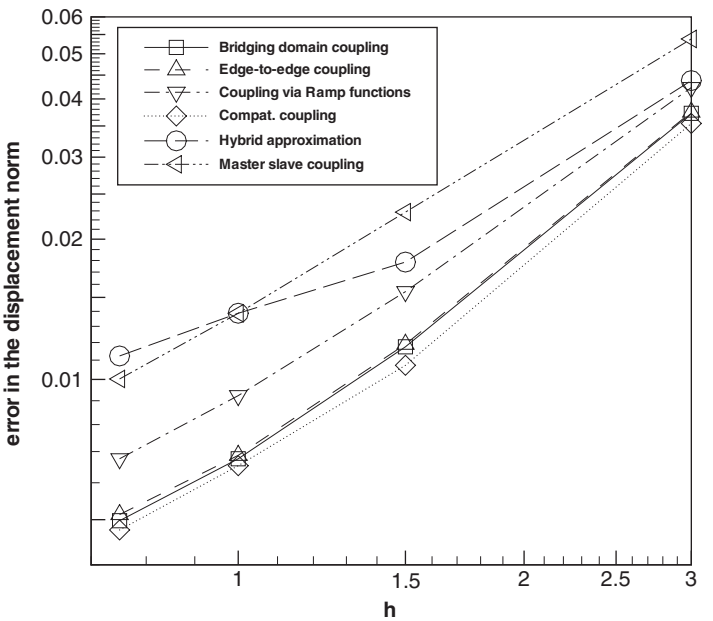

Figure 13. Error in the displacement norm for the different coupling methods for the static Timoshenko beam.

The L_2 error displacement norm is checked in this example

$$L_2 = \frac{\|\mathbf{u}_h - \mathbf{u}_{\text{analytic}}\|}{\|\mathbf{u}_{\text{analytic}}\|} \tag{136}$$

The coupling domain for the Bridging domain coupling in the initial configuration is shown in Figure 12. For the other approaches the particle and the FE-domain do not overlap.

The different coupling methods in Section 5 are studied. Figure 13 shows the error in the displacement norm versus the element length. The best results are obtained from the bridging domain coupling, the edge-to-edge coupling and the compatibility coupling. The differences are marginal. The coupling via ramp functions give similar results in the convergence rate though the absolute error is higher. The worst results are obtained by the master–slave coupling and the hybrid coupling method.

As can be seen from Figure 13 (see also Table II), the convergence rate is decreasing with increasing refinement. Table II lists the values of the convergence rate for the different refinement steps.

6.1.2. Crack-propagation problem. The next example is a crack-propagation problem in concrete. Therefore, a notched beam is loaded as shown in Figure 14. The beam fails due to

Table II. Convergence rates.

	h_1–h_2 (3–1.5)	h_2–h_3 (1.5–1.0)	h_3–h_4 (1.0–0.75)
Bridging domain coupling	1.66	1.365	1.06
Edge-to-edge coupling	1.657	1.354	1.02
Coupling via ramp function	1.455	1.267	1.03
Compatibility coupling	1.72	1.23	1.1
Master–slave coupling	1.23	1.23	1.13
Hybrid coupling	1.23	1.23	1.13

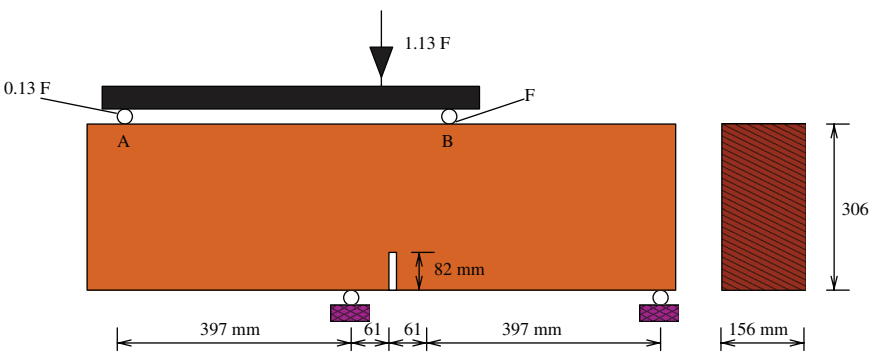

Figure 14. Test set-up of the notched concrete beam of Arrea and Ingraffea [47].

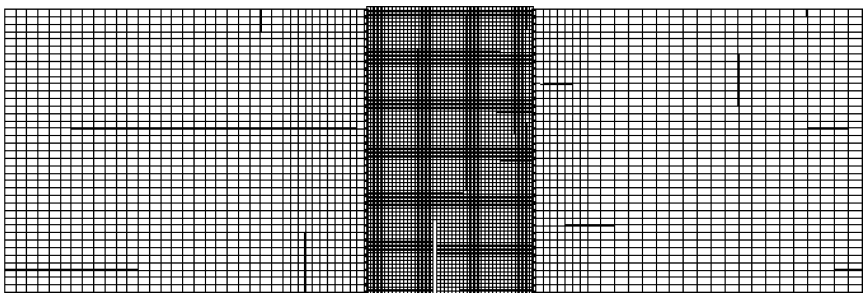

Figure 15. Discretization of the notched concrete beam of Arrea and Ingraffea [47].

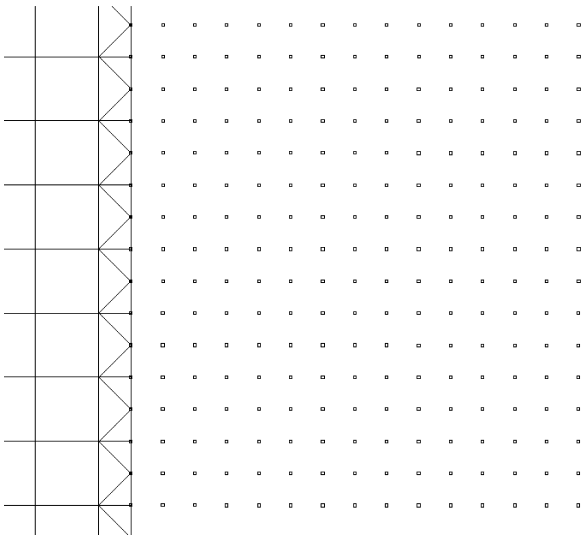

Figure 16. Discretization of the notched concrete beam of Arrea and Ingraffea [47].

a mixed mode failure. Experimental data are available, see Reference [47]. Since particles have advantages over FEs in crack problems, the area around the notch, where we expect the crack to propagate, is discretized with particles while the rest is discretized with a much coarser FE mesh. We have also run computations with a pure mesh-free discretization. The advantage of the hybrid scheme is the lower computational cost.

The results in the crack path are pretty similar for all tested methods. We will show results for the coupling with Lagrange multipliers, the coupling with ramp functions and the master–slave coupling. A typical discretization in the initial configuration is shown in Figure 15. Figure 16 shows the discretization close to the transition between FEs and particles for the case when particles are located directly on FE nodes. We will compare the crack paths and the load–displacement (right of the notch) curves to the experimental data.

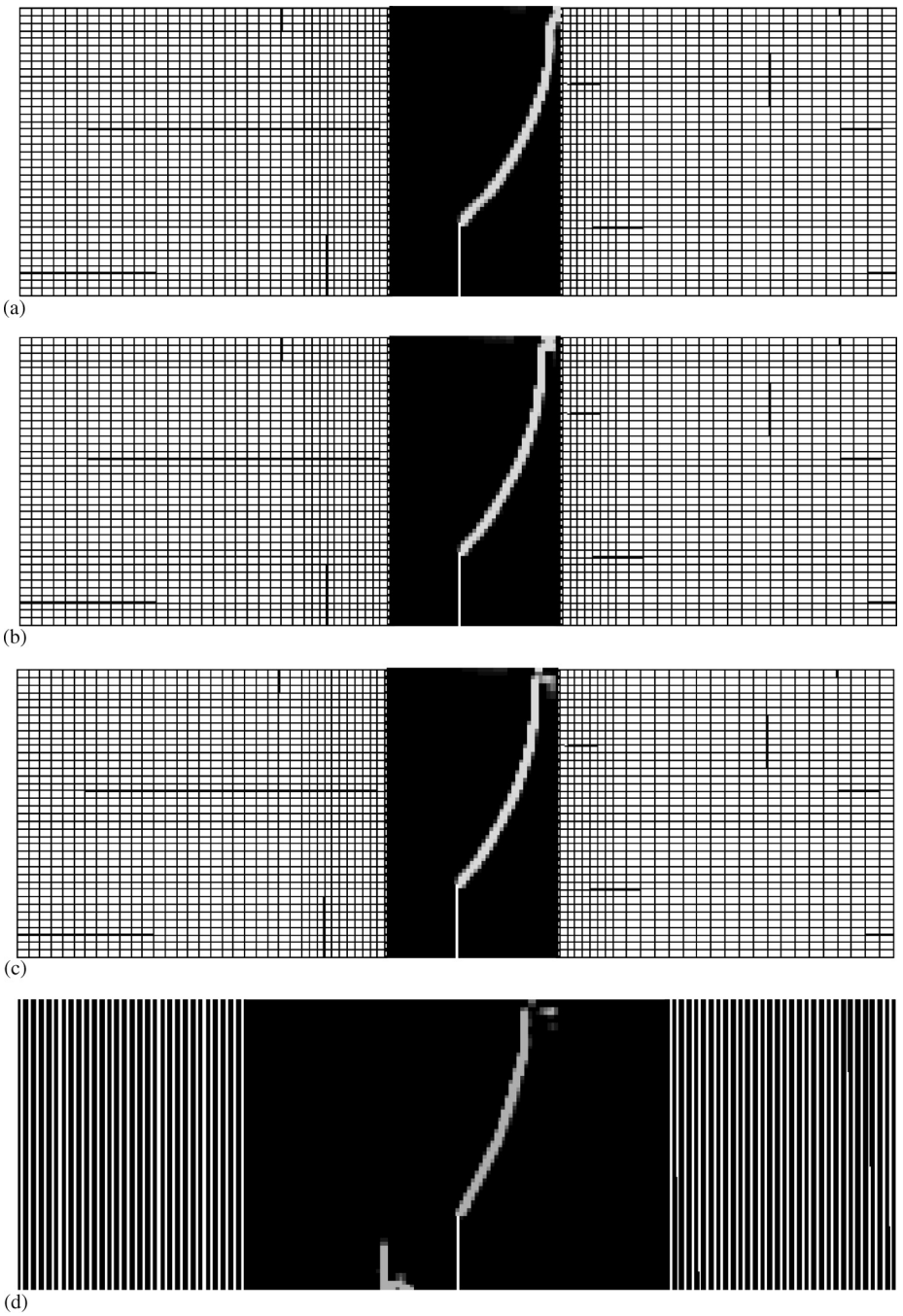

Figure 17. Crack paths for the hybrid coupling: (a) rigid coupling; (b) compatibility coupling; (c) coupling via ramp functions; and (d) pure mesh-free discretization.

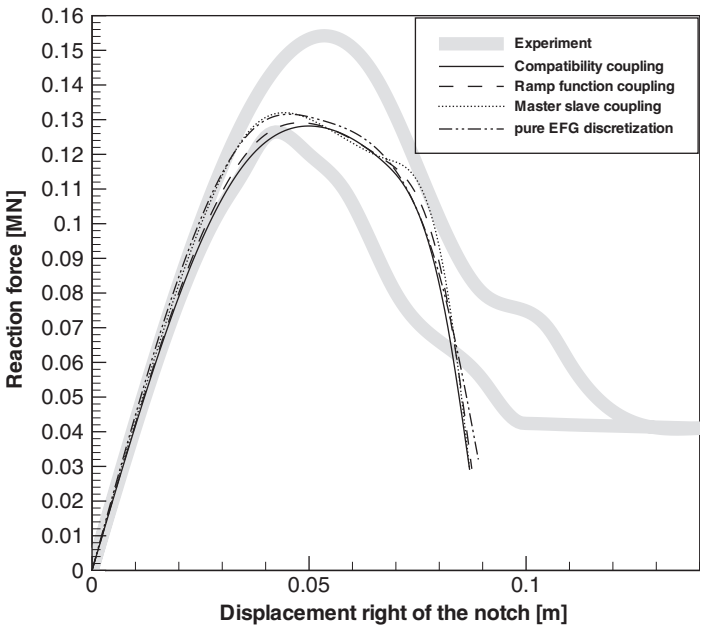

Figure 18. Load–displacement curve of the different computations compared to the experimental data.

We have chosen a combined continuum–discontinuum approach to describe the concrete, see Reference [48]. The concrete is modelled with linear elastic material behaviour in compression and with the Lemaitre model [49] in tension. In the discontinuous region, a linear traction-crack opening relation is applied. Details of this model can be found in Reference [48].

For all hybrid discretization, we will show results for approximately 3500 particles in the region where the crack is expected. The adjacent region is modelled with 2700 elements. Finer meshes gave similar results.

For the pure EFG approximation, the total number of particles is approximately 13 400. The crack paths for the different coupled methods and the pure EFG discretization are shown in Figure 17. The results look very similar but the pure mesh-free discretization is computationally more expensive. A slightly curved crack can be observed which matches well with the experimental results.

The load–displacement (right of the notch) curves are shown in Figure 18. All curves are lying within the experimental scatter and show marginal differences.

6.2. *Dynamic examples*

6.2.1. The rod with initial boundary velocity condition. To investigate the coupling methods for dynamic problems, we consider a linear elastic rod. The rod is discretized in two dimensions (plane strain). It is 60 mm long and its height is 5 mm. An initial velocity of $v = e^{(-\alpha(x-30)^2)}$, $\alpha = 0.025$ is prescribed. The sound speed is $c = \sqrt{E/\varrho}$ with $E = 210\,000$ MPa and $\varrho = 0.0078\,\mathrm{g/mm^3}$, so the wave returns to its original position at $t = 0.011563$ ms. This

Table III. L_2 error in the velocities for an initial condition (Gauss distribution of the velocities) for different methods before and after the wave reflection.

	Error at 0.0116 ms	Error at 0.0231 ms	CPU time (min)
Master–slave coupling	0.0289	0.0465	5.3
Hybrid coupling	0.0141	0.0152	5.5
Coupling via ramp functions	0.0179	0.0323	5.5
Compatibility coupling	0.016	0.03201	5.6
Bridging domain coupling	0.0107	0.0111	5.8
EFG	0.007842	0.007901	9.1

example was studied in Reference [38] for pure particle methods. Xiao [45] showed in one dimension that the bridging domain coupling is superior to other coupling methods in wave reflection problems since spurious wave reflections are removed.

We study different ratios between particles and FE nodes, from 1:1 up to 8:1. We also study the influence of the refinement. Half of the rod is discretized mesh-free while the other part is discretized with FEs as it was done in Section 6.1.1 for the Timoshenko beam. The Young's modulus E is set to 210 000 and the Poisson's ratio is $v = 0.0$. The L_2 error in the velocities is given before and after the wave reflection:

$$\|\mathrm{err}\|_{L_2} = \frac{\|\mathbf{v}^h - \mathbf{v}_{\mathrm{analytic}}\|}{\|\mathbf{v}_{\mathrm{analytic}}\|} \tag{137}$$

Additional to the coupling methods, we will give also the results for a pure mesh-free discretization, i.e. EFG with stress point integration. In Table III, the results are presented for approximately 20 000 nodes+particles and a ratio of 4:1. The error in the velocity is given for the different methods at two times. At $t = 0.011563$ ms, the wave first reaches its original position, at $t = 0.023126$ ms it reaches its original position for the second time.

As can be seen, the best results are obtained by the pure mesh-free discretization. Of course, there is no noise caused due to any coupling. The smallest error is obtained with the bridging domain coupling followed by the hybrid coupling method. The largest error occurs for the rigid coupling. Except for the pure mesh-free discretization and the bridging domain coupling, it can seen that the error increases in time. This increase in error is probably caused by spurious wave reflections. Table III also gives the computation times for the different methods. As can be seen, the mesh-free method gives the most accurate results but the computation time is approximately 2 times longer. It should be mentioned that half of the rod is discretized with particles, so that a dramatic speed up is expected if a smaller fraction of the structure is discretized with particles.

If the ratio between particles and FE nodes is decreased, the error over time in the velocity norm increases in the hybrid method up to a factor of 2 for the tested example and a ratio of 1:1. However, for larger ratios, the hybrid method gives more accurate results than all the other methods tested (except for the bridging domain coupling). The bridging domain coupling also gives a nearly constant error at the two different times for lower ratios.

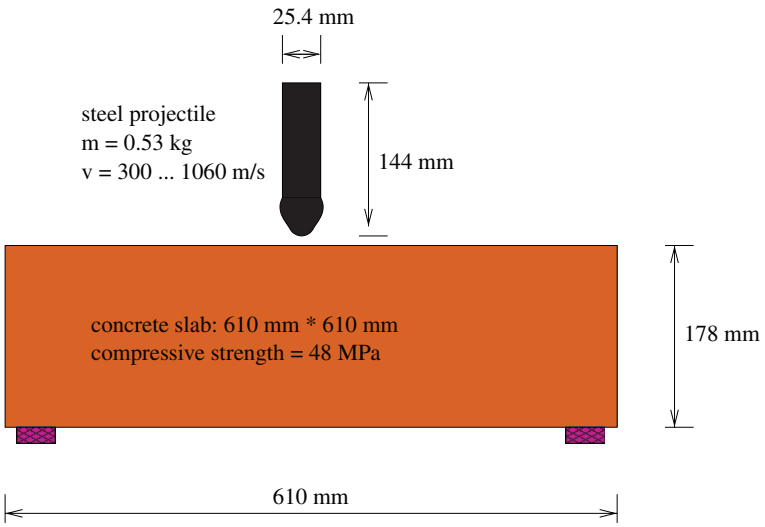

Figure 19. Experimental set-up of the impact experiments preformed by Hanchak *et al.* [50].

6.2.2. Impact of a concrete slab. Hanchak *et al.* [50] performed different impact experiments of reinforced concrete slabs. In their experiments, the concrete had a compressive strength of 48 and 140 MPa, respectively. They used a 0.53 kg steel projectile which was shot onto a 0.178 m thick 0.61 m $\times$ 0.61 m concrete slab, see Figure 19. Besides the initial velocity of the steel projectile, they also measured its discharge velocity. The influence of the reinforcement (5.7 mm diameter, $e = 76$ mm) in respect to the perforation resistance is negligible according to Hanchak *et al.* [50]. Interesting is the observation, that the concrete with a strength of 140 MPa was able to increase the perforation resistance only slightly in respect to the concrete with a compressive strength of 48 MPa. The experimental set-up is shown in Figure 19.

The particle and FE discretization are exemplarily shown for the ramp function coupling, Figure 20. The region where we expect large deformations and a high damage is discretized with particles, the rest is discretized with FEs. We made use of the symmetry and discretized only half of the projectile and the slab. At a discretization of 2520 particles and 836 elements for the concrete, we obtained mesh-independent results which are presented here. The projectile is modelled with a pure FE mesh using 70 elements.

The reinforcement is modelled via an elastoplastic material law with a strain-based failure. Simplified, a rigid bond between concrete and the reinforcement is assumed. For the concrete a constitutive model as described in Reference [51] was used. The initial elasticity modulus for concrete accounts for 36 000 MPa and the compressive strength for 48 MPa. All other material parameters can be found in Reference [51].

As mentioned above, additional to the experimental data, we compare our results to a pure mesh-free (EFG) discretization.

Figure 21 shows the deformed concrete plate at different time steps for the two-dimensional simulation using the ramp function coupling method. Table IV compares the ejection velocity of the Hanchak experiments with different coupling methods and pure mesh-free discretization.

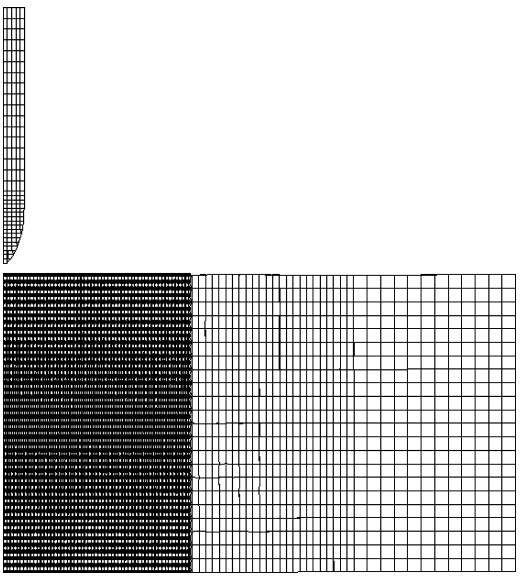

Figure 20. Hybrid discretization of the concrete slab.

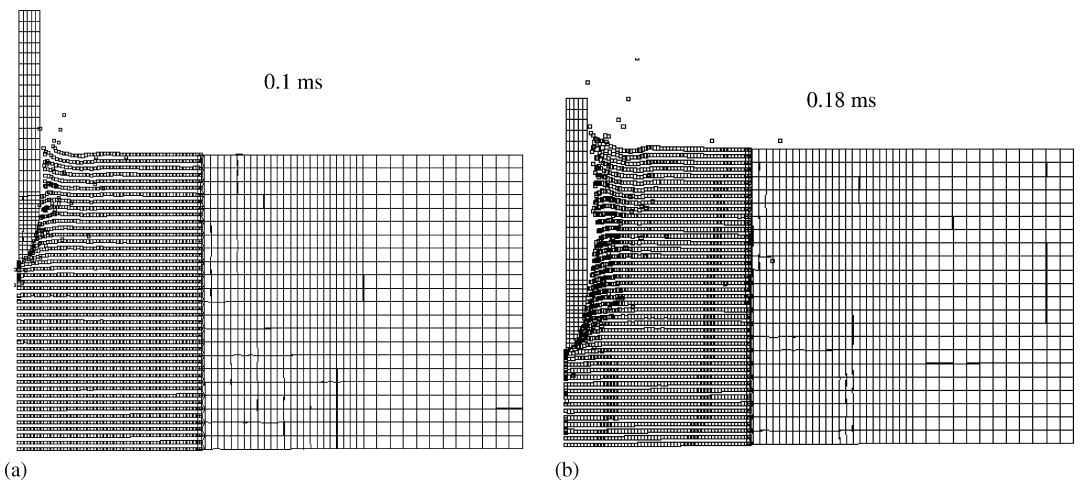

Figure 21. Deformed configuration of the Hanchak slab using the ramp function coupling: (a) at 0.1 ms; and (b) at 0.18 ms.

The coupling methods approximate the measured ejection velocity quite well for high impact velocities. For low impact velocities, larger discrepancies between the hybrid and pure mesh-free approximation can be observed. We cannot explain why there are larger discrepancies for higher impact velocities but we attribute these discrepancies to wave effects at the boundaries. The computation time for the pure mesh-free discretization is approximately 8 times higher

Table IV. Ejection velocities for different impact velocities.

Plate (impact velocity, m/s)	Experiment (m/s)	Ramp function coupling (m/s)	Compatibility coupling (m/s)	Hybrid coupling (m/s)	Master–slave coupling (m/s)	Pure EFG discretization (m/s)
H1 (360)	67	12	22	69	26	76
H2 (430)	214	175	184	207	183	216
H3 (750)	615	604	611	616	611	620
H4 (1060)	947	947	949	948	948	950

than for the coupling methods. The discrepancies in computational costs are marginal between the different methods.

7. SUMMARY AND DISCUSSION

We gave an overview about different particle-finite element coupling techniques; master–slave couplings, coupling via ramp functions, compatibility coupling, bridging domain coupling and hybrid coupling.

Major theme is to use coupled methods due to computational efficiency. Local domains where cracks or large deformations are expected should be discretized with particles while other domains should be discretized with finite elements.

For the cantilever beam problem, we observe, that the master–slave and the hybrid coupling gave the worst results. All other methods showed similar accuracy. All coupling methods gave similar results for the static Arrea–Ingraffea beam problem.

For the rod with initial boundary condition, only the bridging domain coupling and the hybrid coupling method gave a nearly constant error with time. In all other methods, the error increased with time that indicates spurious wave reflection. One drawback of the hybrid method is that the error over time in the velocity norm increases with decreasing ratio of particles to nodes at the interface. However, the hybrid method has the advantage that adaptivity can be incorporated quite easily compared to all other methods and is for large-scale problems such as impacts probably most efficient. At the start, finite elements are used which can be transformed into finite elements. However, one can question if these methods are more accurate than remeshing algorithms since data have to be mapped as in remeshing finite element algorithms. Sauer [20] studied these issues and investigations are still underway.

The best choice for a coupling methods is definitely problem dependent. From the implementational point of view, the master–slave coupling is probably the easiest and the bridging domain coupling is by far the most challenging one to code. For linear elasto-statics, we have observed that the hybrid method and the master–slave coupling gave the worst results. However, when applying these methods to non-linear problems with local cracking, all coupling methods performed similarly well.

For wave propagation problems, only the bridging domain coupling and the hybrid coupling gave sufficient results. In all other methods, the error increased in time. Also comparisons with experimental data and pure mesh-free discretizations indicate that spurious wave reflections influence the results.

Finally, we would like to mention that the different coupling techniques have some typical applications. While the bridging domain method was successfully applied in multi-scale simulations—where often atoms were used instead of particles—as demonstrated by Xiao [45], the compatibility coupling, e.g. was applied to static failure of reinforced concrete structures, [13]. Due to the wide application area, the limit of different numerical methods is not surprising. The development of new coupling method is still a hot topic of ongoing research.

REFERENCES

1. Li S, Liu WK. *Meshfree Particle Methods*. Springer: Berlin, 2004.
2. Attaway SW, Heinstein MW, Swegle JW. Coupling of smoothed particle hydrodynamics with the finite element method. *Post-SMIRT Impact IV Seminar*, Berlin. *Nuclear Engineering and Design* 1994; **150**.
3. Belytschko T, Liu WK, Moran B. *Nonlinear Finite Elements for Continua and Structures*. Wiley: New York, U.S.A., 2000.
4. Johnson GR. Linking of Lagrangian particle methods to standard finite element methods for high velocity impact computations. *Post-SMIRT Impact IV Seminar*, Berlin. *Nuclear Engineering and Design* 1994; **150**.
5. Johnson GR, Stryk RA, Beissel SR. SPH for high velocity impact computations. *Computer Methods in Applied Mechanics and Engineering* 1996; **139**:347–374.
6. Liu WK, Chen Y. Wavelet and multiple scale reproducing kernel particle methods. *International Journal for Numerical Methods in Fluid Dynamics* 1995; **21**:901–931.
7. Liu WK, Uras RA, Chen Y. Enrichment of the finite element method with reproducing kernel particle method. *Journal of Applied Mechanics* 1997; **135**:143–166.
8. Belytschko T, Organ D, Krongauz Y. A coupled finite element-element-free Galerkin method. *Computational Mechanics* 1995; **17**:186–195.
9. Belytschko T, Krongauz Y, Dolbow J, Gerlach C. On the completeness of meshfree particle methods. *International Journal for Numerical Methods in Engineering* 1998; **43**:785–819.
10. Huerta A, Fernandez-Mendez S. Enrichment and coupling of the finite element and meshless method. *International Journal for Numerical Methods in Engineering* 2000; **48**:1615–1636.
11. Huerta A, Fernandez-Mendez S, Liu WK. A comparison of two formulations to blend finite elements and meshfree methods. *Computer Methods in Applied Mechanics and Engineering* 2004; **193**(12–14):1105–1117.
12. Hegen D. Element free Galerkin methods in combination with finite element approaches. *Computer Methods in Applied Mechanics and Engineering* 1996; **135**:143–166.
13. Rabczuk T, Belytschko T. Application of mesh free methods to static fracture of reinforced concrete structures. *International Journal of Fracture* 2006; **137**(1–4):19–49.
14. Karutz H. Adaptive Kopplung der Elementfreien Galerkin Methode mit der Methode der Finiten Elemente bei Rissfortschrittsproblemen. *Dissertation*, Institut fuer Statik und Dynamik der Ruhr Universitaet Bochum, VDI-Verlag, Reihe 18, Band 255, 2000.
15. Belytschko T, Xiao SP. A bridging domain method for coupling continua with molecular dynamics. *Computer Methods in Applied Mechanics and Engineering* 2004; **193**:1645–1669.
16. Wagner GJ, Liu WK. Coupling of atomic and continuum simulations using a bridging scale decomposition. *Journal of Computational Physics* 2003; **190**:249–274.
17. Liu WK, Karpov EG, Zhang S, Park HS. An introduction to computational nanomechanics and materials. *Computer Methods in Applied Mechanics and Engineering* 2004; **193**:1529–1578.
18. Kadowaki H, Liu WK. Bridging multi-scale method for localization problems. *Computer Methods in Applied Mechanics and Engineering* 2004; **193**(30–32):3267–3302.
19. Kadowaki H, Liu WK. A multiscale approach for the micropolar continuum model. *Computer Modeling in Engineering and Sciences* 2005; **7**(3):269–282.
20. Sauer M. Adaptive Koppling des netzfreien SPH-Verfahrens mit finiten Elementen zur Berechnung von Impaktvorgaengen. *Dissertation*, Universitaet der Bundeswehr Muenchen, Institut fuer Mechanik und Statik, 2000.
21. Liu WK, Han W, Lu H, Li S, Cao J. Reproducing kernel element method. Part I: Theoretical formulation. *Computer Methods in Applied Mechanics and Engineering* 2004; **193**:933–951.
22. Li S, Lu H, Han W, Liu WK, Simkins DC. Reproducing kernel element method. Part II: Globally conforming Im/Cn hierarchies. *Computer Methods in Applied Mechanics and Engineering* 2004; **193**:953–987.
23. Simkins Jr DC, Li S, Lu H, Liu WK. Reproducing kernel element method. Part IV: Globally compatible Cn (n1) triangular hierarchy. *Computer Methods in Applied Mechanics and Engineering* 2004; **193**: 1013–1034.

24. Hao S, Liu WK, Belytschko T. Moving particle finite element method with global smoothness. *International Journal for Numerical Methods in Engineering* 2004; **59**(7):1007–1020.
25. Wagner GJ, Liu WK. Hierarchical enrichment for bridging scales and meshfree boundary conditions. *International Journal for Numerical Methods in Engineering* 2001; **50**:507–524.
26. Han W, Wagner GJ, Liu WK. Convergence analysis of a hierarchical enrichment of dirichlet boundary conditions in a mesh-free method. *International Journal for Numerical Methods in Engineering* 2002; **53**(6):1323–1336.
27. Li S, Liu WK. Meshfree and particle methods and their applications. *Applied Mechanics Review* 2002; **55**:1–34.
28. Babuska I, Melenk JM. The partition of unity finite element method. *Technical Note BN-1185*, University of Maryland, 1995.
29. Chen JS, Pan C, Wu CT, Liu WK. Reproducing kernel particle methods for large deformation analysis of nonlinear structures. *Computer Methods in Applied Mechanics and Engineering* 1996; **139**:95–227.
30. Chen JS, Pan C, Roque, CMOL, Wang HP. A Lagrangian reproducing kernel particle method for metal forming analysis. *Computational Mechanics* 1998; **22**:289–307.
31. Duarte CA, Oden JT. Hp clouds—a meshless method to solve boundary-value problems. *TICAM Report 95-05*, 1995.
32. Haeusler-Combe U. *Elementfreie Galerkin-Verfahren*, *Grundlagen und Einsatzmoeglichkeiten*, *Habilitation*. Institut fuer Massivbau und Baustofftechnologie, Universitaet Karlsruhe, 2001.
33. Liu WK, Adee J, Jun S. Reproducing kernel and wavelet particle methods for elastic and plastic problems. In *Advances Computational Methods for Material Modeling*, Benson DJ, Asaro RA (eds), AMD 180 and PVP 268, ASME, 1993; 175–190.
34. Liu WK, Chen Y, Jun S, Chen S, Belytschko T, Pan C, Uras RA, Chang CT. Overview and applications of the reproducing kernel particle methods. *Archives of Computational Methods in Engineering*, *State of the Art Reviews* 1996; **3**:3–80.
35. Liu WK, Jun S, Adee J, Belytschko T. Reproducing kernel particle method for structural dynamics. *International Journal for Numerical Methods in Engineering* 1995; **38**:1665–1679.
36. Liu WK, Jun S, Zhang YF. Reproducing kernel particle methods. *International Journal for Numerical Methods in Fluids* 1995; **20**:1081–1106.
37. Xiao SP, Belytschko T. Material stability analysis of particle methods. *Advances in Computational Mathematics* 2005; **23**:171–190.
38. Rabczuk T, Belytschko T, Xiao SP. Stable particle methods based on Lagrangian kernels. *Computer Methods in Applied Mechanics and Engineering* 2004; **193**:1035–1063.
39. Belytschko T, Lu YY *et al*. Element-free Galerkin methods. *International Journal for Numerical Methods in Engineering* 1994; **37**:229–256.
40. Belytschko T. Crack propagation by element free Galerkin methods. *Engineering Fracture Mechanics* 1995; **51**/**2**:295–315.
41. Belytschko T, Lu YY. Element-free Galerkin methods for static and dynamic fracture. *International Journal of Solids and Structures* 1995; **32**:2547–2570.
42. Gingold RA, Monaghan JJ. Smoothed particle hydro-dynamics: theory and applications to non-spherical stars. *Monthly Notices of the Royal Astronomical Society* 1977; **181**:375–389.
43. Lucy. A numerical approach to the testing of fission hypothesis. *Astronomical Journal* 1977; **82**:1013–1024.
44. Belytschko T, Xiao SP. Stability analysis of particle methods with corrected derivatives. *Computers and Mathematics with Applications* 2000; **43**:329–350.
45. Xiao SP. Atomistic simulations of nanotube fracture and stability analysis of particle methods. *Ph.D. Thesis*, Department of Mechanical Engineering, Northwestern University, 2002.
46. Timoshenko SP, Goodier JN. *Theory of Elasticity*. McGraw-Hill: New York, 1970.
47. Arrea M, Ingraffea AR. Mixed-mode crack propagation in mortar and concrete. *Report No. 81-13*, Department of Structural Engineering, Cornell University Ithaka, NY, 1982.
48. Rabczuk T, Belytschko T. Cracking particles: a simplified mesh-free method for arbitrary evolving cracks. *International Journal for Numerical Methods in Engineering* 2004; **61**(13):2316–2343.
49. Lemaitre J. Evaluation of dissipation and damage in metal submitted to dynamic loading. *Proceedings ICM*, vol. 1, 1971.
50. Hanchak SJ, Forrestal MJ, Young ER, Erhrgott JQ. Perforation of concrete slabs with 48 MPa (7 ksi) and 140 MPA (20 ksi) unconfined compressive strengths. *International Journal of Impact Engineering* 1992; **12**:1–7.
51. Rabczuk T, Eibl J. Simulation of high velocity concrete fragmentation using SPH/MLSPH. *International Journal for Numerical Methods in Engineering* 2003; **56**:1421–1444.

